Journal of The Electrochemical Society, 2021 **168** 050512

A Comparative Study of Structural Changes during Long-Term Cycling of NCM-811 at Ambient and Elevated Temperatures

Benjamin Strehle,[=,*,z] **Franziska Friedrich,**[=,*] **and Hubert A. Gasteiger**[**]

Chair of Technical Electrochemistry, Department of Chemistry and Catalysis Research Center, Technical University of Munich, D-85748 Garching, Germany

Lithium-ion batteries operate predominantly at room temperature, but some applications such as electric vehicles also demand operation at higher temperature. This is especially challenging for cathode active materials (CAMs), which undergo an accelerated failure at elevated temperature. Here, we systematically compare the capacity fading of the Ni-rich NCM-811 at two different temperatures. The first dataset over 1000 cycles at 22 °C stems from a former study, while the NCM-811/graphite full-cells are investigated now under similar conditions at 45 °C for 700 cycles. We focus on the CAM by using pre-lithiated graphite anodes. The capacity loss due to NCM-811 degradation at 45 °C is more than doubled compared to 22 °C. The underlying mechanisms related to the bulk and the surface of the CAM are quantified by several ex situ techniques such as X-ray powder diffraction, half-cell cycling with impedance spectroscopy, and Kr-BET. The aging happens mainly at the surface of the primary particles, forming a resistive, disordered surface layer, whose thickness is estimated to reach ≈6 nm at 22 °C and ≈12–14 nm at 45 °C by the end-of-test. Furthermore, the Li-Ni mixing in the bulk increases by ≈1%–2% at elevated temperature, but its contribution to the capacity loss remains elusive.

 [DOI: 10.1149/1945-7111/abf780]

Manuscript submitted February 25, 2021; revised manuscript received March 29, 2021. Published May 13, 2021. *This was Paper 254 presented during PRiME 2020, October 4–9, 2020.*

Layered transition-metal oxides are the most widely applied class of cathode active materials (CAMs) in lithium-ion batteries (LIBs). They dominate the fast-growing market of electric vehicles (EVs), combining high energy and power density with long cycle-life.[1] On a structural level, layered oxides can be written as $Li_{1+\delta}[TM]_{1-\delta}O_2$, with alternating layers of lithium and transition-metals (TMs) in octahedral coordination and with a small degree of over-lithiation (typically $0 < \delta < 0.05$). Depending on the choice of transition-metals, layered oxides are referred to as NCMs (combining Ni, Co, and Mn) or NCAs (replacing Mn by Al, which is actually not a TM). Making efforts to reduce the cobalt content due to sustainability and geopolitical aspects,[2,3] there is an ongoing trend to increase the nickel content as much as possible. This strategy goes along with a higher specific capacity at a given cell voltage compared to less Ni-rich counterparts, but Ni-rich CAMs are also prone to structural and thermal instabilities.[4,5] In this respect, NCM-811 ($Li_{1+\delta}[Ni_{0.8}Co_{0.1}Mn_{0.1}]_{1-\delta}O_2$) is currently one of the most Ni-rich NCM materials with proven cycling stability.[6–8]

In a recent study from 2019, we investigated the long-term cycling stability of NCM-811 at ambient temperature (≈22 °C).[9] Using in situ X-ray powder diffraction (XPD) in combination with other diagnostics such as electrochemical impedance spectroscopy (EIS) and X-ray photoelectron spectroscopy (XPS), we elucidated the capacity fading mechanism of an NCM-811 cathode active material and quantified its main contributions to cell capacity fading over the duration of 1000 cycles. We provided evidence that the high-voltage operation until 4.5 V vs Li^+/Li leads to the formation of a resistive, oxygen-depleted surface layer around the primary particles. Consequently, the capacity fading intrinsic to the NCM-811 CAM can be divided into two contributions, one originating from the irreversible cathode active material loss (due to the surface reconstruction of the CAM) and one originating from the growing charge-transfer resistance and the associated overpotential loss (due to the resistive nature of the surface layer). The latter is particularly pronounced at high charge/discharge rates.

Even though the majority of applications are designed to operate at/near room temperature, there is a growing demand for lithium-ion batteries to operate and survive also under more extreme thermal conditions.[10,11] Electric vehicles, e.g., should run both in colder and hotter regions. The United States Advanced Battery Consortium (USABC) aims at a survival temperature ranging from −40 °C to +66 °C for 24 h.[12] This goal for EV applications might be one of the reasons why the focus of academic research is increasingly placed on performing cycling studies at elevated temperatures (in the range of ≈40 °C–60 °C).[13–16] Furthermore, high-temperature cycling accelerates the battery failure and can thus be used as an accelerated stress test (AST) to evaluate new or optimized CAMs. Alternative AST strategies that have been reported are potential hold or open circuit voltage (OCV) rest phases at high voltages as well as cycling with low salt concentrations.[17]

On the other hand, the evaluation of ASTs requires facile characterization methods to extract important battery parameters over the course of (long-term) cycling. With respect to CAM evaluation, such parameters are the percentage of active material loss and the increase of the charge-transfer resistance, which were deduced from in situ XPD and EIS in our former work. In situ and operando techniques can generate much more authoritative information than ex situ (or post-mortem) experiments, because they characterize the material under real operating conditions. At the same time, they are often cumbersome and need advanced instrumentation (e.g., custom-made cell designs or synchrotron radiation), which is not readily available in every laboratory. Thus, high-throughput ASTs should be accompanied by some basic ex situ techniques.

In the present work, we want to systematically compare the long-term cycling performance of NCM-811 at ambient and elevated temperatures. Using the cycle-life analysis over 1000 cycles at 22 °C from our precedent study as Ref. 9, the same NCM-811 cathode active material is cycled here at 45 °C for up to 700 cycles. To ensure comparability, the other cycling conditions are kept constant. As in our previous study, the graphite counter-electrode (CE) is pre-lithiated to eliminate cell capacity fading contributions from the anode and the NCM-811 potential is controlled vs the lithium reference-electrode (RE). Every ≈150 cycles, one of the pouch cells is stopped and the harvested cathode electrode is subjected to several ex situ techniques such as XPD, EIS, and surface area determination

[=]These authors contributed equally to this work.
[*]Electrochemical Society Student Member.
[**]Electrochemical Society Fellow.
[z]E-mail: benjamin.strehle@tum.de

by Kr-BET. Here, the NCM-811 cathode active material loss is quantified by two independent approaches, either by XPD or purely by electrochemical means, while the charge-transfer resistance from EIS is compared to direct current internal resistance (DCIR) measurements in the pouch cells. Furthermore, we are seeking to clarify whether the NCM-811 CAM aging at elevated temperature is mechanistically similar, or different, to its fading at ambient temperature. This question addresses the relative importance of bulk vs surface related degradation phenomena, in particular Li-Ni mixing in the bulk vs surface reconstruction.

Experimental

Battery assembly and cycling.—The materials and battery design used here are identical to our previous aging study of NCM-811 at ambient temperature and can be looked up in detail there.[9] Briefly, the CAM composition was determined to be $Li_{1.01}Ni_{0.79}Co_{0.10}Mn_{0.10}O_2$ by elemental analysis, which gives a theoretical capacity of 274 mAh g^{-1} (including ≈2.2 wt% surface impurities). Cathode electrode sheets with 94 wt% CAM, 2 wt% Timcal SFG6L graphite, 1 wt% Timcal C65 conductive carbon, and 3 wt% Kynar PVDF binder (HSV900) were provided by BASF SE (Germany). The electrode sheets were calendered to a porosity of ≈30% and have a CAM loading of ≈7.0 mg_{CAM} cm^{-2} (±1%), corresponding to ≈1.4 mAh cm^{-2} for a practical capacity of 200 mAh g^{-1}. The CAM loading is lower than the previously reported value of ≈7.4 mg_{CAM} cm^{-2}, probably due to a small variation along the electrode spool. Single-layer pouch cells with 9 cm^2 cathode area (30 × 30 mm^2) were manufactured with a geometrically as well as capacitively over-sized graphite counter-electrode (CE, 33 × 33 mm^2, ≈7.1 $mg_{graphite}$ cm^{-2}, corresponding to ≈2.3 mAh cm^{-2}, BASF SE), two glass-fiber (GF) separators (36 × 36 mm^2, glass microfiber filter 691, VWR, Germany), a lithium metal reference-electrode (RE), and 700 µL LP57 electrolyte (1M $LiPF_6$ in EC:EMC = 3:7 by weight; electrolyte-to-CAM mass ratio of ≈13/1). In contrast to our former study that used LP57-2 with 2% vinylene carbonate (VC), the VC additive was omitted in the full-cells in this work due to its oxidative instability at elevated temperatures.[18] To ensure a stable solid electrolyte interface (SEI), the graphite counter-electrode was however pre-formed and pre-lithiated in a half-cell configuration at 45 °C in LP57-2 electrolyte. The pre-lithiation to ≈$Li_{0.24}C_6$ (corresponding to ≈0.55 mAh cm^{-2}) provides a sufficiently large lithium reservoir for the full-cells (0.55/1.4 ≈ 40% of the cathode capacity). This approach avoids any capacity fading due to the loss of cyclable lithium and thus, the Li-RE can be used for the potential control of the cathode. Furthermore, the anode/cathode balancing after pre-lithiation amounts to (2.3-0.55)/1.4 ≈ 1.25/1, i.e., the remaining storage capability of the anode does not pose a risk for lithium plating during charge. The pouch cells were compressed in a spring-loaded holder at a homogeneous pressure of ≈2 bar.

The pouch cells were tested at 45 °C in a temperature-controlled chamber (Binder, Germany) with a battery cycler (Series 4000, Maccor, USA). The cycling protocol consists of a loop of 50 cycle segments, which are further divided into three sequential steps:

(i) The first two cycles were done at constant-current (CC) mode at a C-rate of C/10 and in the cathode potential window of 3.0–4.5 V vs Li^+/Li, as controlled vs the Li-RE. All C-rates throughout this study are based on a nominal specific capacity of 200 mAh g^{-1} and the unit "V" refers to 'V vs Li^+/Li', unless stated otherwise.

(ii) The third cycle is a direct current internal resistance (DCIR) measurement at a relative state of charge (SOC) of 65%, as referenced to the discharge capacity of the preceding C/10 cycle. The partial charge to 65% SOC, where the DCIR measurement was taken, and the subsequent discharge back to a cathode potential of 3.0 V were also carried out at C/10. The DCIR measurement itself was done after a 2 h rest period at open circuit voltage (OCV, ≈4.0 V), applying a discharge pulse of C/5 for 10 s. The area specific resistance (R_{DCIR} in Ω cm^2) was computed by the Maccor MIMS Client according to:[19]

$$R_{DCIR} = \frac{\frac{V_1 + V_3}{2} - V_2}{j_2} \quad [1]$$

Here, V_1 is the OCV right before the pulse, V_2 is the voltage at the end of the 10 s pulse, V_3 is the OCV 10 s after the pulse, and j_2 is the current density of the C/5 discharge pulse (≈0.28 mA cm^{-2}). Please note that the induced change of ≈0.1 mAh g^{-1} (corresponding to an SOC variation of ≈0.05%) is negligible and that R_{DCIR} relates solely to the resistance of the cathode due to the potential control vs the Li-RE.

(iii) The remaining 47 cycles were done in CC mode at C/2 between cathode potentials of 3.0–4.5 V, which are, for the sake of comparability, the same cycling conditions than in our previous study at ≈22 °C.[9]

This iterative protocol of 50 cycle segments was applied to six cells, which passed through an increasing total number of cycles, ranging from only six cycles (i.e., two cycles at C/10, one DCIR test cycle, and three cycles at C/2; referred to as begin-of-test, BOT), to 100 cycles and then in steps of 150 cycles to a maximum of 700 cycles (end-of-test, EOT). Each cell was stopped in the discharged state (i.e., after a final C/2 cycle until 3.0 V) and the cathode OCV was measured for ≈5 h at 45 °C and finally for another ≈5 h at 25 °C. The final OCV values taken at 45 °C and 25 °C agree within less than ±10 mV for a given cell. After cell disassembly, the NCM-811 cathode electrodes were stored for further ex situ analyses in an argon-filled glove box.

X-ray powder diffraction and Rietveld refinement.—XPD measurements aimed at monitoring the evolution of the lithium content (x_{Li} in $Li_xNi_{0.79}Co_{0.10}Mn_{0.10}O_2$) and the Li-Ni mixing ($Ni_{Li}$) in the NCM-811 CAM upon cycling. The experiments were conducted at our in-house STOE STADI P diffractometer (STOE, Germany) in transmission mode, using Mo-$K_{\alpha 1}$ radiation (0.7093 Å, 50 kV, 40 mA), a Ge(111) monochromator, and a Mythen 1K detector with one data point every 0.015°/2θ. A silicon standard material was used for the determination of the instrumental broadening. The CAM powder was measured ex situ in air-tight sealed 0.3 mm borosilicate capillaries in the 2θ range of 5°–90° for ≈17 h. For measurements with the discharged CAM, the material was scratched off with a scalpel from the harvested electrodes of each of the six pouch cells and loaded into two capillaries without further washing (for two independent XPD repeat measurements). On the other hand, for measurements with the charged CAM, the 30 × 30 mm^2 cathodes harvested from the cycled pouch cells were punched out into disk-shaped electrodes with a diameter of 14 mm. These smaller electrodes were assembled with a Ø 15 mm Li-CE, two Ø 16 mm GF separators, and 80 µl LP57 electrolyte in CR2032-type coin cells, which were cycled at C/2 and 45 °C for 1.5 cycles between 3.0–4.5 V and then stopped at 4.5 V. Due to electrolyte residuals, the CAM mass could not properly be determined and we used the average loading of the pristine electrodes instead, which leads to an uncertainty of ≈1% for the applied current and the extracted capacity. In order to minimize self-discharge effects, which would lead to an apparently erroneous increase of the determined x_{Li} value in the charged state at 4.5 V, the OCV periods at 45 °C and 25 °C that followed these 1.5 cycles were not longer than 30 min each (change in the OCV at 25 °C of less than 15 mV over the max. 30 min). Afterwards, the coin cells were immediately opened and the charged CAM was prepared for the XPD measurement at the same day.

The Rietveld refinements were performed with the software package Topas.[20] NCM-811 exhibits a layered α-$NaFeO_2$-type

structure with $R\bar{3}m$ symmetry and we therefore used the following structural model: $[Li_{x-v}Ni_v]_{3a}[Li_vNi_{0.79-v}Co_{0.10}Mn_{0.10}]_{3b}[O]_{6c}$. Here, the overall lithium content (x_{Li}) was calculated according to the c/a lattice parameter ratio of the cycled samples. The calibration curves, $x_{Li} = f(c/a)$, were determined by operando XPD from the initial cycles of this particular CAM in our previous publication and they look as follows in the discharged (i.e., at low SOC, $0.62 \leqslant x_{Li,dis} \leqslant 0.91$) and charged state (i.e., at high SOC, $0.12 \leqslant x_{Li,cha} \leqslant 0.23$):[9]

$$x_{Li,dis} = \frac{73.80 - \sqrt{c/a \cdot 10^4 - 49222}}{58.36}, \quad \text{for } 0.62 \leqslant x_{Li,dis} \leqslant 0.91 \qquad [2]$$

$$x_{Li,cha} = \frac{c/a - 4.733}{1.41}, \text{ for } 0.12 \leqslant x_{Li,cha} \leqslant 0.23 \qquad [3]$$

The Li-Ni mixing was treated as a paired anti-site defect ($v_{Li} = v_{Ni}$). This means that the amount of Ni in the Li layer (Ni_{Li}) is the same as the amount of Li in the TM layer (Li_{TM}). Please note that in the special case of the pristine CAM, v_{Li} equals $v_{Ni} + 0.01$ due to full occupation of all layers (at $x_{Li} = 1.01$). The Li-Ni mixing is reported in percentage terms as $Ni_{Li} = v_{Ni} \cdot 100\%$.

The refinements included the following non-structural parameters:

- background: Chebyshev polynomial with 15 parameters
- instrument: zero shift and axial divergence
- absorption: cylindrical absorption correction ($\mu R \approx 0.75$, assuming a packing density of 40%)

The structure-related refinement parameters are the following:

- scale factor
- broadening: isotropic contribution from crystallite size and anisotropic contribution from microstrain using the hexagonal Stephens model[21]
- lattice parameters: a and c
- fractional coordinate: $z_{6c,O}$
- atomic displacement parameters: three site-specific and isotropic parameters ($b_{3a,Li}$, $b_{3b,TM}$, and $b_{6c,O}$)
- site occupancy factors: v_{Ni} (and x_{Li}) as outline above, using ionic scattering factors for all elements (Li^+, Ni^{3+}, Co^{2+}, Mn^{4+}, and O^{2-})

Furthermore, the 2 wt% of conductive graphite (Timcal SFG6L) in the cathode electrode sheet were included into the Rietveld fits by refining its scale factor, crystallite size broadening, and lattice parameters, while fixing the other structural parameters of the $P6_3/mmc$ graphite phase to the values from Dolotko et al.[22] Due to the high intensity of the freshly replaced Mo source, we also noticed tiny reflections of the borosilicate capillary in some of the diffractograms, which were treated as additional reflections based on an empty capillary measurement.

Rate test and impedance analysis.—We punched out another Ø 14 mm electrode from each of the pouch cell cathodes harvested after cycling, reassembling them into coin cells with a lithium metal counter-electrode (separator and electrolyte as described above). These were used to perform a rate test towards slow C-rates in combination with electrochemical impedance spectroscopy (EIS). Since a conventional lithium metal foil would have a large contribution to the EIS response of the NCM-811 half-cells, we placed a free-standing graphite (FSG) electrode on top of the lithium metal foil (i.e., between the lithium metal and the separator), as it was described by Morasch et al.[23] Using this Li/FSG composite as counter-electrode, its impedance contribution (imaginary and real part of $<5\ \Omega\ cm^2$ over the measured frequency range[23]) to the half-cell impedance is comparably small compared to that of the NCM-811 cathode. Consequently, the measured cell impedance can be reasonably well approximated to correspond to that of the NCM-811 cathode. The coin cells were cycled between 3.0–4.5 V at 45 °C for two cycles each at C/2, C/10, C/50, and finally again at C/2. The two C/10 cycles over the entire voltage range were completed by a third DCIR-like cycle to 65% SOC (OCV of ≈4.0 V, see full-cells), at which we conducted potential-controlled EIS measurements with a potentiostat (VMP300, BioLogic, France) in the frequency range of 100 kHz to 100 mHz with an AC voltage perturbation of 15 mV (taking eight data points per decade and three repetitions per point).

To fit the impedance spectra acquired at 65% SOC and 45 °C, we used an equivalent circuit described by R_{HF} + TLM[R_{ion}, R_{CT}/Q_{CT}] + $R_{contact}/Q_{contact}$, with the elements defined as follows: (i) R_{HF} being the high-frequency resistance of the half-cell; (ii) TLM representing a transmission line model with the ionic resistance in the electrolyte phase between the pores of the electrode (R_{ion}), and a parallel circuit element of the charge-transfer resistance (R_{CT}) and a constant phase element (CPE, Q_{CT}); and, (iii) another parallel circuit element of the contact resistance ($R_{contact}$) and a $Q_{contact}$ CPE that is generally observed as an interfacial resistance between the cathode electrode and the aluminum current collector.[9,24] The last discharge of the half-cells at C/2 was to a cell voltage of 2.55 V, followed by constant voltage hold for 1–6 h before cell disassembly. The harvested electrodes were used for surface area measurements that are described in the following.

Surface area determination.—After the rate test, the discharged NCM-811 cathodes were subjected to Kr-BET measurements. Before that, the electrodes were thoroughly washed in three steps with an EC/EMC mixture and twice with DMC to remove any residuals from the conductive salt, as described by Oswald et al.,[25] and then dried at 120 °C under dynamic vacuum for at least 6 h. Surface area measurements were performed on a gas sorption analyzer (Autosorb-iQ, Quantachrome, USA) at 77 K using krypton as adsorbate and the obtained surface areas are referenced to the mass of the washed electrodes. Kr has the advantage over N_2 to be much more sensitive due to its ≈300 times lower saturation pressure (p_0), which minimizes the void volume correction and thus enables the analysis of low surface area samples. The specific surface area of the NCM-811 CAM ($A_{BET,CAM}$ in m^2/g_{CAM}) was determined from adsorption isotherms in the relative pressure range of $\approx 0.13 < p/p_0 < 0.29$ with seven data points according to the Brunauer-Emmet-Teller (BET) theory. The actually measured surface area of the entire electrode ($A_{BET,elec}$ in m^2/g_{elec}), consisting of 94 wt% CAM and 6 wt % inactive electrode additives (viz., 2 wt% SFG6L conductive graphite, 1 wt% C65 conductive carbon, and 3 wt% PVDF binder), was converted into $A_{BET,CAM}$ by subtracting the contribution of the inactive electrode additives ($A_{BET,add}$ in m^2/g_{add}):

$$A_{BET,CAM} = \frac{A_{BET,elec} - 0.06 \cdot A_{BET,add}}{0.94} \qquad [4]$$

Here, $A_{BET,add}$ of the overall 6 wt% inactive electrode additives was measured separately, using electrodes comprising only the additives in the same ratio as in the actual NCM-811 electrodes. The pristine additives-only electrode yielded a specific surface area of 5.10 ± 0.11 m^2/g_{add} (average from two electrodes). To evaluate a possible change of $A_{BET,add}$ during cycling, we tried to mimic the full-cell conditions by cyclic voltammetry at a scan rate of 0.2 mV s^{-1} between 2.55–4.5 V (requiring a time comparable to that for C/2 cycling). After 10 or 20 cyclic voltammetry cycles at 45 °C vs a Li/FSG-CE, $A_{BET,add}$ rises by ≈9% to 5.56 ± 0.01 m^2/g_{add} (average from these two cells). Using the specific surface area of the conductive additive powders (SFG6L: ≈20 m^2/g, C65: ≈62 m^2/g), one would expect $A_{BET,add}$ to be ≈17 m^2/g_{add} for the additives-only electrode. This discrepancy is explained by prior observations that pore blocking by the PVDF binder can substantially lower the electrode surface area, depending on the type of conductive additives and the binder content.[25,26] In Eq. 4, the first $A_{BET,add}$ value

($5.10\ m^2/g_{add}$) was used for the pristine NCM-811 electrode, while the latter ($5.56\ m^2/g_{add}$) was used for any cycled electrode. The inactive electrode additives contribute with ≈15%–20% to the total surface area of the cycled electrodes.

Results and Discussion

Electrochemical full-cell data.—To focus solely on the intrinsic degradation mechanisms of the NCM-811 cathode active material at elevated temperature, we designed the full-cells in such a way that common degradation processes originating from the anode and from the electrolyte are effectively suppressed during battery operation. Since the graphite anode is pre-lithiated to a cathode capacity of ≈40% (see Experimental section), the loss of cyclable lithium on the anode side does not contribute to the observed capacity fading.[27] This approach allows the NCM-811 cathode to be operated between fixed cut-off potentials of 3.0 and 4.5 V vs Li^+/Li, as controlled vs a Li-RE. Furthermore, electrolyte changes such as oxidation reactions at the cathode side and $LiPF_6$ salt depletion could deteriorate the cell performance[28] at realistic mass ratios of $m_{electrolyte}/m_{CAM} \approx 1/1$.[29] Therefore, we employ highly porous glass-fiber separators in our full-cells, which enable a large electrolyte excess of $m_{electrolyte}/m_{CAM} \approx 13/1$, so that the bulk electrolyte properties remain unaltered. Assuming that electrolyte degradation is relevant under the applied conditions, the thereby released protic species could lead to transition-metal dissolution from the CAM surface;[27] however, the SiO_2-containing GF separator acts as a proton scavenger.[30,31] We want to stress that all these modifications distinguish this work from other studies using more realistic cell setups (i.e., graphite anode not pre-lithiated, less electrolyte volume, and polyolefin separators), but they are done on purpose to obtain an in-depth and quantitative understanding of the CAM degradation. To enhance its degradation processes, the NCM-811 CAM is further subjected to an accelerated stress test, because the upper cut-off potential of 4.5 V vs Li^+/Li is chosen deliberately higher than in commercial NCM/graphite cells. Here, the upper full-cell voltage (V_{FC}) typically amounts to 4.2–4.3 V_{FC},[12,16] corresponding only to ≈4.3–4.4 V vs Li^+/Li.

Figure 1 shows from top to bottom the evolution of the discharge capacity at C/2 (including checkup cycles at C/10), the charge-averaged mean charge and discharge voltage, and the DCIR resistance measured at a relative state of charge (SOC) of 65% (based on the preceding C/10 cycle). For all six cells, the first charge at C/10 to 4.5 V yields ≈237 mAh g^{-1} (not shown), corresponding to an absolute SOC of ≈86% (referenced to the total amount of lithium in the NCM-811 CAM). This is well beyond the onset of oxygen evolution from the layered oxide surface at ≈80%.[32,33] The following C/10 discharge yields a capacity of ≈221 mAh g^{-1}, which decreases to an initial discharge capacity of ≈207 mAh g^{-1} at the faster rate of C/2 (see Fig. 1a). The capacity fading is very reproducible among the six cells, which were tested for an increasing number of cycles ranging from 6 to 700 cycles (see differently colored symbols in Fig. 1a). In the overlapping cycling segments, the average standard deviation between the cells amounts to ±2 mAh g^{-1}.

Focusing first on the C/2 cycling, Table I compares the begin-of-test (BOT) discharge capacity values at 45 °C with those from our previous study with the same CAM at 22 °C as well as their end-of-test (EOT) values after 1000 and 750 cycles, respectively. The BOT capacity increases by ≈24 mAh g^{-1} when comparing the BOT value after 18 cycles at 22 °C and after 6 cycles at 45 °C (for an explanation why BOT was defined after 18 cycles in our previous study, see Ref. 9) or by ≈17 mAh g^{-1} when comparing cycle 6, which we ascribe to the enhanced kinetics at elevated temperature. However, the higher initial capacity at 45 °C goes along with a faster degradation upon cycling, with the capacity fading of ≈0.04 mAh g^{-1} per cycle at 22 °C being more than doubled at 45 °C (≈0.10 mAh g^{-1} per cycle). Consequently, the EOT capacity of ≈139 mAh g^{-1} after 700 cycles at 45 °C is already ≈6 mAh g^{-1} lower than that after 1000 cycles at 22 °C.

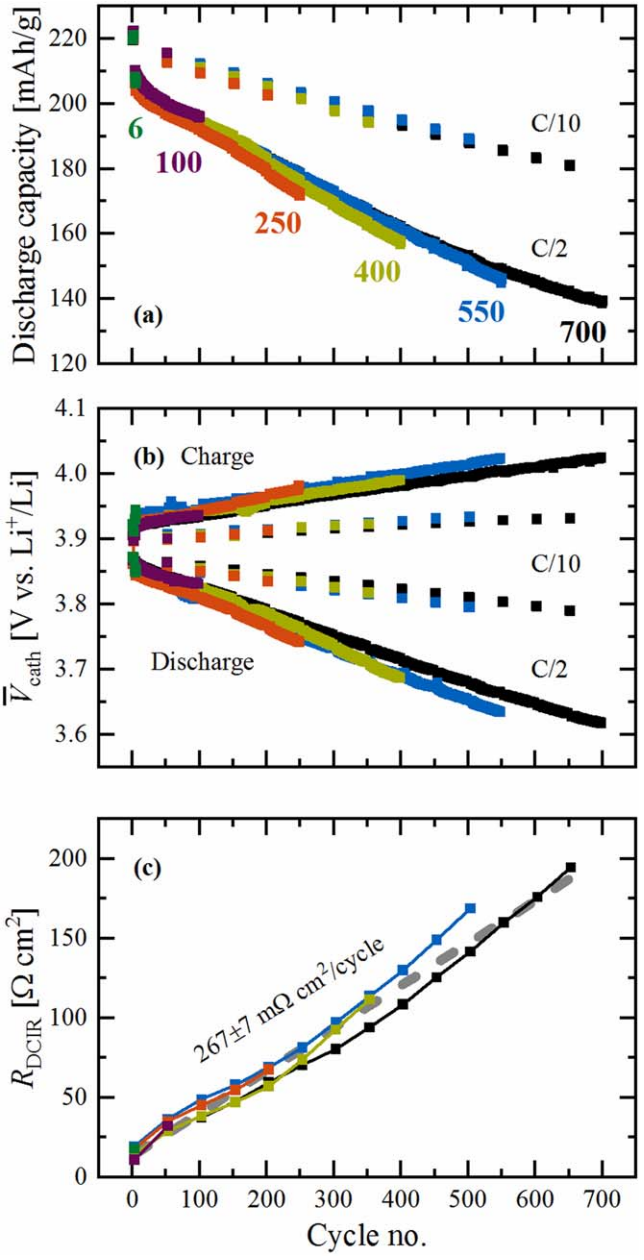

Figure 1. Cycle-life degradation of the NCM-811 CAM evaluated in NCM-811/graphite full-cells with a partially pre-lithiated graphite CE, which were cycled at 45 °C and C/2 (with intermittent C/10 checkup cycles) between cathode potentials of 3.0–4.5 V measured vs a Li-RE. (a) Specific discharge capacities. (b) Charge-averaged mean charge and discharge cathode voltages vs Li^+/Li ($\bar{V}_{cath} \equiv \int V_{cath}\, dq / \int dq$). (c) Cathode resistance measured by a DCIR pulse at 65% SOC with respect to the preceding C/10 cycle (R_{DCIR} calculated according to Eq. 1). The discharge capacities and the mean voltages are shown for both the regular C/2 cycles and the intermittent C/10 checkup cycles, while the DCIR cycles to 65% SOC are excluded from these panels. Slight deviations from the characteristic mean voltage curves due to the change of C-rate or OCV periods were further omitted from panel (b). The numbers in panel (a) give the total number of cycles for each of the six cells. The increase of R_{DCIR} in panel (c) was determined to be 267 ± 7 mΩ cm^2/cycle by a linear fit through all data points, as marked by the dashed gray line ($R^2 = 0.975$).

Even though there is no study which investigates NCM-811 under similar conditions, it is useful to compare our results with literature data in order to validate that the performance degradation shown in Fig. 1a is reasonable. Li et al. tested $LiNi_{0.80}Co_{0.15}Al_{0.05}O_2$ (NCA) in multi-layer pouch cells at 40 °C and various full-cell (FC)

Table I. Comparison of the C/2 discharge capacity, as reported in our previous publication at 22 °C[9] and as measured in this work at 45 °C. The NCM-811/graphite full-cells were cycled between cathode potentials of 3.0–4.5 V vs Li^+/Li and analyzed from the respective begin-of-test (BOT) to end-of-test (EOT).

C/2 capacity [mAh g^{-1}]	Ambient temperature (22 °C)	Elevated temperature (45 °C)
BOT → EOT	Cycle 18 → 1000	Cycle 6 → 700
BOT	≈183	≈207
EOT	≈145	≈139
Capacity loss ($\Delta C_{EC}^{BOT\rightarrow EOT}$)	≈38 (≈0.04 per cycle)	≈68 (≈0.10 per cycle)
Capacity retention	≈79%	≈67%

cut-off conditions, including C/2 cycling between 3.0–4.2 V_{FC} and 3.0–4.3 V_{FC} with a constant voltage (CV) hold at the upper cut-off.[13] Please note that the full-cell voltage (V_{FC}) is roughly 0.1 V lower than the cathode potentials vs Li^+/Li given in our study and that we use a partially pre-lithiated graphite CE. After 700 cycles of these NCA/graphite full-cells, the capacity retention amounts to ≈86% (at an upper cathode potential of ≈4.3 V vs Li^+/Li) and ≈78% (≈4.4 V vs Li^+/Li), which is more than the ≈67% obtained for our NCM-811/graphite full-cells under the slightly harsher conditions of 45 °C and an upper cathode potential of 4.5 V vs Li^+/Li (see Table I). Schweidler et al. investigated NCM-851005/graphite single-layer pouch cells at 45 °C and 1C between 2.8 and 4.2 V_{FC} (also with CV hold, CE not pre-lithiated).[15] They report an initial capacity of ≈195 mAh g^{-1} and a fairly linear fading of ≈0.07 mAh g^{-1} per cycle. Since the capacity loss is again smaller than in our present work, it is reasonable to assume that the CAM aging, which strongly increases with increasing upper cathode potentials, is the dominant factor in all cases, and that any lithium inventory loss at the anode does not contribute much to the reported fading. In realistic full-cells, the amount of cyclable lithium could be reduced, e.g., due to TM dissolution from the cathode and the consequent attack of the SEI,[34] which potentially limits the lithiation of the CAM during discharge.[35] Here, the pre-lithiation of the graphite anode deliberately eliminates this effect in order to focus on the degradation of the NCM-811 CAM.

The ex situ diagnostic analyses presented later will try to answer the question if the aging mechanism of the NCM-811 CAM is mostly due to its surface reconstruction, as it was the case in our previous degradation study with the same CAM conducted at 22 °C,[9] or if other (bulk) phenomena come into play at an elevated temperature. The reduced fading of ≈0.06 mAh g^{-1} per cycle during the C/10 checkup cycles compared to ≈0.10 mAh g^{-1} per cycle at C/2 (both taken from Fig. 1a) already points towards an overpotential-induced capacity loss, which might be caused by the formation of a resistive surface layer and/or by an increase of the bulk resistance of the CAM (e.g., due to sluggish lithium diffusion kinetics). Such a resistance build-up is further suggested by the evolution of the mean charge and discharge cathode voltages shown in Fig. 1b. Inspecting their average changes over cycling (see Table II), the decrease of the mean discharge voltage is always higher than the increase of the mean charge voltage (by a factor of 1.5–2.5). This discrepancy could potentially be ascribed to a path dependence of the cathode resistance (or one of its components) between charge and discharge. In this context, Pan et al. reported the chemical diffusion coefficient of Li ($\tilde{D}_{Li}$) to be up to four times higher during delithiation (i.e., during charge) than during lithiation (i.e., during discharge) of $LiCoO_2$ thin-film electrodes at the H1-H2 phase transition.[36] This initial phase transition takes place at low SOCs, where also NCM layered oxides exhibit largely different resistances: while the voltage vs capacity curve is relatively flat at the beginning of charge, indicating small overpotentials, it drops steeply at the end of discharge, i.e., the cathode resistance is much higher for the same lithium content during discharge.[9,13] Besides the lithium diffusion kinetics in the bulk of the CAM, the charge-transfer resistance at its surface might also contribute to the different changes of the cathode mean voltage during charge vs discharge (see Table II). The charge-transfer rises strongly towards the voltage cut-offs, especially at the low-SOC limit, which makes it however difficult to clearly resolve differences between charge and discharge under common measurement conditions (e.g., for EIS measurements with a capacity spacing of 20 mAh g^{-1}).[9]

Finally, Fig. 1c shows the evolution of the direct current internal resistance (R_{DCIR}) of the cathode, which was measured in the mid-SOC range (65% SOC based on the preceding C/10 cycle), so that it is only marginally affected by slight variations of the lithium content (x_{Li}) upon cycling: this relative SOC of 65% occurs within the narrow OCV range of 3.98–4.00 V over all cycles, indicating a small variation of x_{Li}, and furthermore lies in a region where the charge-transfer resistance varies little with x_{Li} (note that R_{CT} is at/near its minimum at an OCV of ≈4.0 V for any given cycle, as shown in Fig. 6 of our previous study with the same CAM[9]). Here, R_{DCIR} rises almost linearly for all six cells (see Fig. 1c), with an average slope of 267 ± 7 mΩ cm^2 per cycle. This resistance increase can also be translated into a voltage change by multiplying the slope with the current densities applied at C/2 and C/10, respectively. Doing so in Table II, the calculated voltage changes of ≈0.19 and ≈0.04 mV/cycle resemble the evolution of the mean charge voltage, amounting to ≈0.14 mV/cycle at C/2 and ≈0.05 mV/cycle at C/10, whereas the evolution of the mean discharge voltages stays higher. This might be due to the fact that the mean discharge voltage is dominated by the very high R_{CT} (and/or very low $\tilde{D}_{Li}$) at low SOCs, so that R_{DCIR} taken near the minimum of the R_{CT} vs SOC curve is not representative of the much higher resistance toward the end of discharge.

Validation of the DCIR measurement by EIS.—Since the DCIR measurement does not tell us which component(s) of the cathode resistance increases upon cycling, we performed an ex situ EIS analysis with the harvested pouch cell electrodes. To enable this analysis in a coin cell setup, i.e., in the absence of a μ-RE, the Li-CE was extended by a free-standing graphite (FSG) electrode in contact with metallic lithium, which drastically lowers the impedance of the counter-electrode.[23] The coin cells with such a Li/FSG-CE ran through a multi-step cycling procedure, which includes an EIS measurement at a relative SOC of 65% within a DCIR-like cycle, analogous to that conducted with the full-cells (see Experimental section for more details). The results of the EIS analysis are illustrated in Fig. 2.

First, the feasibility of this approach was tested with a symmetrical cell of two Li/FSG electrodes, which was cycled similarly to the actual coin cells (by applying the same current densities and charging times). As shown in Fig. 2a, the imaginary part of the impedance of such a symmetrical Li/FSG cell is below ≈1 Ω cm^2 and the HFR-corrected real part of its impedance is below ≈5 Ω cm^2 (sum of both electrodes), consistent with the values reported in Ref. 23. As will be shown below, these impedances are very small compared to the HFR-corrected impedances of the coin cells composed of harvested NCM-811 cathodes and a Li/FSG-CE, so that the HFR-corrected impedance response of the latter closely corresponds to the impedance of the harvested NCM-811 electrodes.

Table II. Comparison of the mean voltage change of the NCM-811 cathode ($\bar{V}_{cath}$) during C/2 and C/10 cycling at either 22 °C over 1000 cycles or at 45 °C over 700 cycles. For charge and discharge, the slope from linear fits of the mean voltages presented in our previous publication[9] and in Fig. 1b is given in absolute values. Furthermore, the mean voltage change was calculated from R_{DCIR} in Fig. 1c according to $\frac{d\bar{V}_{cath}}{dcycle} = \frac{dR_{DCIR}}{dcycle}\Delta j$, with $\frac{dR_{DCIR}}{dcycle} = 267\ m\Omega\ cm^2/cycle$ and j = 0.7 mA cm^{-2} at C/2 and 0.14 mA cm^{-2} at C/10, respectively.

$\frac{d\bar{V}_{cath}}{dcycle}$ [mV/cycle]	Ambient temperature (22 °C) C/2 cycling	Elevated temperature (45 °C)	
		C/2 cycling	C/10 cycling
Charge	≈0.08	≈0.14	≈0.05
Discharge	≈0.12	≈0.35	≈0.11
Discharge/charge ratio	≈1.5	≈2.5	≈2.2
From R_{DCIR}	n.d.	≈0.19	≈0.04

More precisely, the contribution of the Li/FSG-CE to the overall impedance would even be lower since the symmetric Li/FSG cell impedance represents the impedance of two rather than one Li/FSG electrodes.

The spectra in Fig. 2 feature two semicircles: (i) a small semicircle at high frequencies (with a frequency maximum of $f_{max} \approx$ 2.2–5.4 kHz between 6 and 700 cycles), and (ii) another semicircle at low frequencies (with $f_{max} \approx$ 14.8-0.18 Hz between 6 and 700 cycles), whose diameter increases significantly upon cycling. As illustrated in our previous publications,[9,37] the underlying processes that are represented by each of the two *R*/*Q* elements in our impedance model (see caption of Fig. 2) can be deduced from an estimate of the associated double layer capacitance, which normalized to the proper interface should be on the order of 10 μF cm^{-2}.[24] Doing so, the high-frequency semicircle must correspond to the contact resistance between the cathode electrode coating and the current collector, since its capacitance when normalized to the geometric surface area of the current collector results in 2–4 μF/cm$^2_{geom}$. The low-frequency semicircle on the other hand is described by a transmission line model (TLM) that represents a complex convolution of the ion conduction in the electrolyte phase within the porous electrode (R_{ion}) and the charge-transfer resistance (R_{CT}). Its capacitance should thus reflect the double layer capacitance of the CAM and the conductive additives, consistent with the fact that the capacitance normalized by the BET surface area of the cycled cathode electrodes results in 10–25 μF/cm$^2_{BET}$. Here, the surface area of the cycled electrodes amounts to $A_{BET,elec} \approx$ 1.6–2.8 m^2/g$_{elec}$, as determined by Kr-BET (see Experimental section).

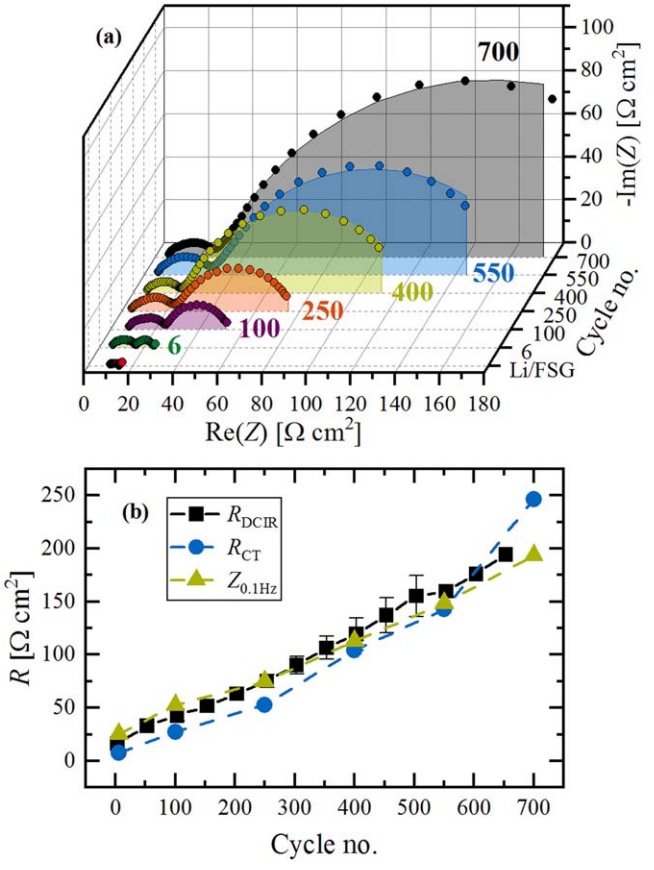

Figure 2. Ex situ EIS analysis of the harvested pouch cell cathodes, from which 14 mm diameter electrodes were punched out and re-assembled as working-electrode (WE) vs a Li/FSG-CE in a coin cell. (a) Impedance spectra were measured at the same conditions as the DCIR pulse in the full-cells (45 °C, 65% SOC, OCV ≈ 4.0 V). The data points (symbols) were fitted (lines) to: R_{HF} + TLM[R_{ion}, R_{CT}/Q_{CT}] + $R_{contact}/Q_{contact}$. The spectrum of a symmetrical Li/FSG cell, which underwent the same cycling procedure than the other coin cells prior to the EIS measurement, is also shown, demonstrating the negligible contribution of the Li/FSG-CE to the overall impedance beyond the high-frequency resistance. (b) Comparison of the averaged R_{DCIR} from Fig. 1c with the cathode charge-transfer resistance (R_{CT}) determined from the above fit of the EIS data and the low-frequency impedance at 0.1 Hz ($Z_{0.1Hz}$).

The contact resistance ($R_{contact}$) deduced from the high-frequency semicircle is in the range of ≈12–26 Ω cm^2. The observed small variation of this value might be caused by artifacts from the assembly of the coin cells with harvested cathodes. The α value of the corresponding constant phase element ($Q_{contact}$) is on the order of ≈0.7. The low-frequency semicircle was fitted by a transmission line model, consisting of R_{ion} and R_{CT}/Q_{CT}.[24] The values for R_{ion} are ≈0.75–1.5 Ω cm^2 for the samples up to 250 cycles. Afterwards, as the charge-transfer resistance becomes very large, the deconvolution of R_{ion} and R_{CT} becomes rather error-prone, resulting in fitted R_{ion} values of ≈10–20 Ω cm^2, which is likely incorrect. For cathode electrodes with ≈30% porosity, as used in this study, we do not expect that R_{ion} significantly increases over cycling. Thus, for the fitting of the impedance spectra where a reasonable value for R_{ion} could not be determined due to the dominance of R_{CT} (after 400–700 cycles), we used a fixed value of 1.5 Ω cm^2 for R_{ion}. The α value of Q_{CT} evolves gradually from 0.93 to 0.75. For these cycling data at 45 °C, R_{CT} increases from ≈7 Ω cm^2 after 6 cycles to ≈246 Ω cm^2 after 700 cycles. This is considerably higher than at 22 °C, where R_{CT} for the same CAM amounted to ≈100–150 Ω cm^2 after 1000 cycles,[9] which indicates the formation of a thicker resistive surface layer at elevated temperature.

In Fig. 2b, the R_{CT} values obtained from the fit of the EIS data of the harvested NCM-811 cathodes (see Fig. 2a) are compared to the averaged R_{DCIR} values of the six full-cells (data taken from Fig. 1c). Note that the DCIR pulse was conducted every 50 cycles at the beginning of the full-cell cycling loop, so that the last measurement was taken after 650 cycles, while the ex situ EIS measurements are taken up to 700 cycles. The charge-transfer resistance of the NCM-811 cathode fully describes the observed R_{DCIR} trend, with R_{CT} increasing in a similar fashion as R_{DCIR}. The observation that R_{CT} is consistently lower than R_{DCIR} is due to the fact that the latter also includes contributions from R_{HF}, $R_{contact}$, and R_{ion}. Therefore, a more rigorous comparison of the DCIR resistance with the EIS data would be to compare it with the EIS-derived low-frequency resistance, which corresponds to the magnitude of the impedance

Table III. Rietveld refinement results of the NCM-811 CAM (pristine CAM powder, pristine electrode, as well as cycled and discharged electrodes). For the cycled electrodes, one of the two separately measured capillaries of the same electrode is exemplary given in the table (viz., the measurement with the lower Ni_{Li} value). The table summarizes quality factors (*R*-values), lattice parameters, and the therefrom determined Li content (according to Eq. 2 for the cycled electrodes), atomic site-specific information (including Li-Ni mixing, fractional z-coordinate of O, and atomic displacement parameters), and the fitted weight fraction of conductive graphite (nominally 2 wt%). Errors are given in parenthesis.

	Pristine powder	Pristine electrode	6	100	250	400	550	700
R_{wp} [%]	3.68	2.45	4.09	4.01	3.94	4.19	4.11	4.38
R_{bragg} [%]	0.906	0.648	0.898	0.989	1.06	1.30	1.12	1.55
χ^2	2.46	1.35	3.79	3.61	3.49	4.16	4.41	4.48
a [Å]	2.87214(1)	2.87246(1)	2.86888(2)	2.86873(2)	2.86738(2)	2.86690(2)	2.86606(2)	2.86693(2)
c [Å]	14.2081(1)	14.2080(1)	14.2409(1)	14.2516(1)	14.2622(2)	14.2712(2)	14.2735(2)	14.2756(2)
c/*a* [–]	4.94685(5)	4.94629(5)	4.96391(5)	4.96790(6)	4.97395(6)	4.97792(6)	4.98017(6)	4.97939(7)
x_{Li} [–]	1.01	1.01	0.915	0.898	0.875	0.861	0.852	0.855
Ni_{Li} [%]	1.98(7)	1.84(7)	1.71(8)	2.13(8)	2.54(8)	3.07(8)	2.75(8)	3.54(9)
$z_{6c,O}$ [–]	0.24113(5)	0.24092(5)	0.24029(6)	0.24016(6)	0.24011(6)	0.24000(7)	0.23993(6)	0.24006(7)
$b_{3a,Li}$ [Å^2]	0.73(5)	0.68(6)	0.76(8)	0.73(7)	0.80(8)	0.80(8)	0.85(8)	0.81(8)
$b_{3b,TM}$ [Å^2]	0.310(4)	0.473(5)	0.462(6)	0.482(6)	0.479(6)	0.432(7)	0.489(7)	0.445(7)
$b_{6c,O}$ [Å^2]	0.81(1)	0.97(2)	1.07(2)	1.12(2)	1.18(2)	1.23(2)	1.16(2)	1.25(2)
Graphite [wt%]	n.d.	1.9(1)	1.56(8)	1.44(8)	1.29(9)	1.47(9)	1.32(9)	1.30(9)

($|Z| = \sqrt{\mathrm{Re}(Z)^2 + \mathrm{Im}(Z)^2}$) at the nominal equivalent frequency than the DCIR pulse duration. For the here used 10 s DCIR pulse, this translates into 100 mHz, which is the lowest frequency measured during EIS analysis shown in Fig. 2a. Therefore, the magnitude of the impedance at 100 mHz ($Z_{0.1Hz}$) is compared with R_{DCIR} in Fig. 2b. R_{DCIR} and $Z_{0.1Hz}$ agree within ±10 Ω cm^2 throughout cycling, which is quite reasonable. For the first data points after 6 and 100 cycles, $Z_{0.1Hz}$ is slightly higher than R_{DCIR}, which most likely is due to the fact that the two more cycles at C/2 and C/10 that were applied to the harvested cathode electrodes prior to the ex situ EIS measurements might add some additional aging to the relatively fresh NCM-811 CAM.

Even though we believe that the here measured charge-transfer resistance predominantly originates from a reconstructed, spinel/rock-salt-type surface layer, which is caused by oxygen release and which grows from the CAM surface gradually into its interior, there is also the possibility that electrolyte decomposition products might form a resistive surface film, which is often referred to as cathode-electrolyte interphase (CEI).[11] This CEI-type surface film would grow on top of the CAM surface. The high-frequency semicircle obviously does not allow for discerning the occurrence of two different types of surface layers; however, we can try to evaluate the importance of the CEI on the basis of (i) the electrochemical stability of the electrolyte towards anodic oxidation and (ii) its chemical stability towards reactive lattice oxygen.[38] Regarding the first point, Metzger et al. have shown that EC-based electrolytes are oxidatively stable at potentials greater than 4.5 V vs Li^+/Li, even at an elevated temperature of 50 °C.[39] This is further supported by an LNMO study by Pritzl et al.,[18] where LNMO/graphite full-cells were cycled at 40 °C and with an LP57 electrolyte containing different concentrations of VC. LNMO is an ideal model electrode, because the spinel structure is inherently stable against oxygen release and the concomitant surface reconstruction.[33,38] At the same time, it operates at a high potential of ≈4.7 V vs Li^+/Li, which enables to study exclusively the influence of electrolyte oxidation on the cathode resistance. For the EC/EMC/$LiPF_6$ base electrolyte without VC, the cathode resistance remained constant over the duration of 100 cycles, i.e., we can exclude the formation of a resistive CEI-type surface layer. If VC was added in high concentrations, the cathode resistance however increased because VC gets already oxidized at ≈4.3 V vs Li^+/Li, so that an organic film of poly(VC) deposits on the LNMO surface. For this reason, VC was omitted in our NCM-811/graphite full-cells.

The oxygen release from the CAM surface is accompanied by the chemical degradation of the electrolyte.[40] In case of EC, the attack of singlet oxygen leads to the in situ formation of VC at an intermediate stage of the decomposition cascade. When NCM-622/graphite full-cells are cycled above the onset potential of oxygen release (until 4.6 V_{FC} at 25 °C), Teufl et al. reported a rapid rollover failure within ≈25 cycles using an EC-based electrolyte and a low $m_{electrolyte}/m_{CAM}$ ratio of ≈1.6/1.[41] The authors suggested that the cell resistance build-up that leads to this rollover failure is due to an increase of the cathode resistance, caused by the oxidation of VC at these high potentials. On the other hand, the capacity fading of very similar NCM-622/graphite cells with LP57 electrolyte (also cycled until 4.6 V_{FC} at 25 °C) is considerably less using a $m_{electrolyte}/m_{CAM}$ ratio of ≈8/1.[14] Here, the cells last for ≈300 cycles until they reach the same capacity drop than after the above rollover failure. In summary, we cannot entirely exclude the formation of a resistive CEI-type surface film also in our case, especially at the elevated temperature of 45 °C, where both the oxygen release and the electrolyte decomposition are increased compared to 25 °C operation.[14] However, the here used ≈0.2 V lower upper cut-off potential of 4.5 V vs Li^+/Li and the higher $m_{electrolyte}/m_{CAM}$ ratio of ≈13/1 probably counteract these effects. Furthermore, we think that such an organic surface film, if present, does not contribute to the observed capacity losses, because its share in R_{CT} is expected to be independent of the state of charge (and thus not larger than measured for the medium SOC of 65% in Fig. 2). On the other hand, R_{CT} significantly increases towards the lower and upper SOC limit at the cut-off voltages,[9] which is believed to be caused by the slowed Li diffusion within the reconstructed, spinel/rock-salt-type surface layer.[42]

Bulk stability and Li-Ni mixing analyzed via XPD.—The bulk stability of layered oxides typically refers to the level of cation mixing, where a transition-metal moves irreversibly from the native TM layer into the Li layer. Due to similar ionic radii of Li^+ and Ni^{2+}, Ni is mainly believed to be the moving TM,[4,43,44] but X-ray diffraction does not allow any distinction among the three TMs and Ni is just the most favorable representative in the investigated Ni-rich NCM-811. Refining the Li-Ni mixing as a paired anti-site defect of Ni_{Li} and Li_{TM} in the common $R\bar{3}m$ space group, we observed no systematic change in the extent of Li-Ni mixing between the pristine and EOT samples after 1000 cycles in our prior study with the same CAM at 22 °C.[9] We thus concluded that the freely refined Ni_{Li} stays constant at a level of ≈3%, which was recently supported by Xu et al. for NCM-811 also cycled at room temperature.[45] The Rietveld refinement results of the present study at 45 °C are summarized in Fig. 3 and Table III.

Figure 3a shows exemplarily the XPD pattern of the discharged cathode at EOT after 700 cycles and the corresponding Rietveld

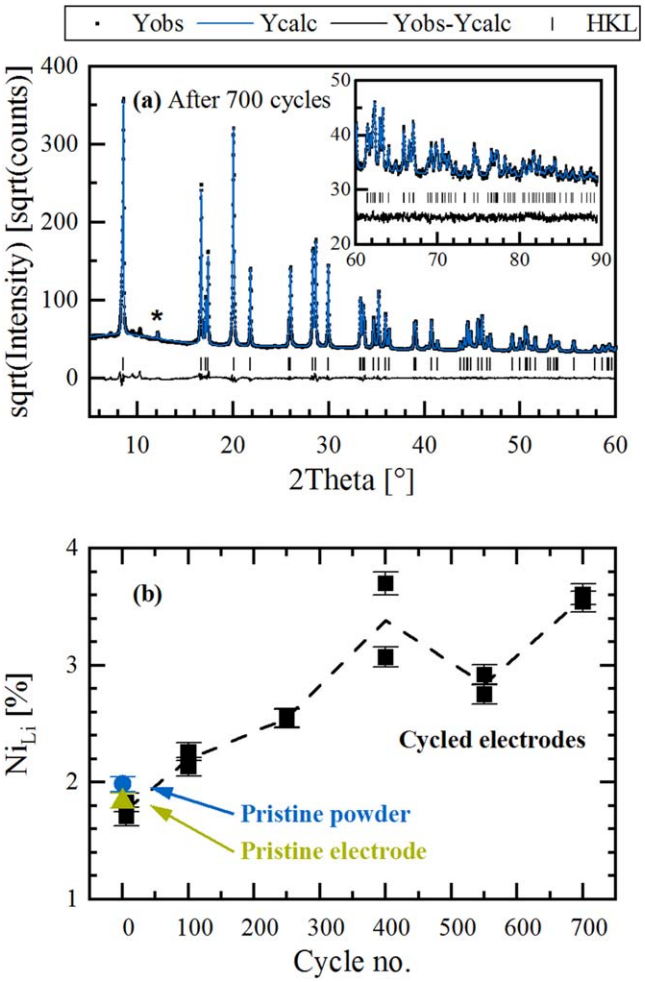

Figure 3. Determination of the Li-Ni mixing from ex situ XPD data of the harvested NCM-811 electrodes in the discharged state. (a) Rietveld refinement of the EOT NCM-811 CAM after 700 cycles. The data were collected at our in-house Mo-diffractometer ($\lambda = 0.7093$ Å) in the 2θ range of 5°–90°. The observed (black points), calculated (blue line), and difference diffraction profile (black line) are shown together with the position of the Bragg peaks of NCM-811 (black ticks). The asterisk at ≈12° indicates the strongest (002) reflection of conductive graphite, which was also included into the refinement. The inset shows the high-angular range from 60° to 90°. To visualize the increasingly smaller reflections at higher 2θ, the intensity is displayed on a square root scale on the y-axis. (b) Evolution of the Li-Ni mixing, labeled as Ni_{Li}, over the course of 700 cycles. The cycled electrodes were measured twice in two separate capillaries and are further compared with the pristine CAM powder and the pristine electrode (both heated at 120 °C prior to loading the material into the capillaries). The dashed black line shows the average trend of the cycled electrodes.

refinement fit. Apart from 2 wt% conductive graphite in the electrode formulation, whose most intense peak is highlighted by an asterisk, there is no crystallographic side phase visible in the pattern. Regarding the NCM-811 material, its layered structure is well preserved and the applied model satisfactorily describes the bulk material, as can be also seen from the fairly constant *R*-values in Table III. Other structural parameters such as the atomic displacement parameters scatter in a sufficiently narrow range, which gives further confidence about the validity of the refined Ni_{Li} values (see Fig. 3b).

Ni_{Li} was determined from two separate capillaries of the same harvested cathodes, together with the pristine CAM powder and the pristine electrode. The deviation between the duplicate measurements amounts to less than 0.2%, which is close to the estimated standard uncertainty from the Rietveld fit of ≈0.1%. Only the XPD data from the cathode harvested after 400 cycles differ in this respect with a deviation of ≈0.6%. Starting with the pristine CAM, its Li-Ni mixing of ≈1.8%–2.0% turns out to be lower than the ≈3.1% reported in our previous study, despite using the identical NCM-811 sample and the same electrode sheets that had been stored under inert conditions in an argon-filled glove box. In comparison to the former study, we extended the 2θ range from 60° to 90°, but this does not alter the refinement outcome (within the margin of uncertainty); it only slightly reduces the extent of correlations for the sensitive Ni_{Li} parameter (≈70% to the scale factor and to $b_{3a,Li}$). Unfortunately, we cannot provide a solid explanation for this discrepancy. We speculate that the replacement of the Mo-source and the following re-adjustment of the diffractometer might have caused this difference in the refinement-based value of Ni_{Li}. To avoid any artefacts which might be caused by instrumental variations, we consequently tried to measure the samples in this study under fairly constant conditions within a short period of time. Yin et al. investigated 17 pristine NCM samples by high-resolution X-ray and neutron powder diffraction and they established a linear correlation between the Ni_{Li} amount and the Ni content of the NCM (more specifically, between % Ni_{Li} and Ni^{2+}).[46] For NCM-811, this correlation projects a Ni_{Li} amount of 3.4 ± 0.5%, which would match the value reported in our earlier study.[9] However, as discussed by the authors, the Li-Ni mixing further depends on the calcination temperature and the activation energy of defect formation (on the order of 200–300 meV), so the here reported value of ≈1.8%–2.0% is not unreasonable.

Analyzing the cycled NCM-811 electrodes with regards to Ni_{Li}, we find that for the cathode harvested after only 6 cycles, the extent of Li-Ni mixing agrees with that of the pristine CAM powder and the pristine electrode (see Fig. 3b). After increasingly more cycles, the Li-Ni mixing rises by ≈1%–2% until the end-of-test (700 cycles), depending on how one interprets the scatter of the Ni_{Li} values between 400, 550, and 700 cycles. At this point, we want to discuss shortly some aspects of the structural model: $[Li_{x-v}Ni_v]_{3a}[Li_vNi_{0.79-v}Co_{0.10}Mn_{0.10}]_{3b}[O]_{6c}$ (see also Experimental section). Here, x_{Li} was deduced from the *c*/*a* lattice parameter ratio according to Eq. 2, whereby x_{Li} of the discharged cathodes decreases upon cycling (see Table III). If x_{Li} would have been fixed to the pristine value of 1.01 for all samples (e.g., in default of a proper method to determine x_{Li} of cycled samples), the fitted value of Ni_{Li}, e.g., at EOT (700 cycles) would be reduced from ≈3.6% to ≈2.4% (so that one might mistakenly conclude there is hardly any change in comparison to ≈1.8%–2.0% of the pristine NCM-811). This is due to the fact that the required electron density of the Li layer would mainly be compensated by Li itself, so that there would be no need in the refinement routine to place additional Ni there. Alternatively, refining the Li-Ni mixing not as a paired anti-site defect of Ni_{Li} and Li_{TM}, but purely as Ni_{Li} (i.e., $v_{Li} = 0$), has not such a big impact: the absolute amount of Ni_{Li} would shift to lower values by a maximum of only ≈0.3% after 700 cycles (because the remaining Li again partially provides the required electron density of the Li layer). It is thus very important to report all relevant aspects of the refinement, including a clear description what x_{Li} value was used for a given fit), in order to enable a comparison of the structural data reported in different publications.

Even though the absolute values of Ni_{Li} have to be treated with caution, we are quite confident that the observed trend of an increasing Li-Ni mixing by ≈1%–2% while cycling NCM-811 for 700 cycles at 45 °C between cathode potentials of 3.0–4.5 V is correct. The trickier question, however, addresses the impact of an increasing extent of Li-Ni mixing on the electrochemical performance of the NCM-811 CAM. How would it affect the cathode resistance and finally the achievable capacity? Makimura et al. synthesized a series of $[Li_{1-y}Ni_y][Ni,Co,Al]O_2$ samples ($0 \leqslant y \leqslant 0.13$) and they found a perfectly linear correlation between the capacity (*C*) and *y* for C/10 cycling at 20 °C between cathode potentials of 2.5 and 4.2 V, namely C [mAh g^{-1}] = 181.4 – 725.5·*y*.[47] When normalized to the highest capacity for $y = 0$ (C_0), this

equates to C/C_0 [%] = 100 – 400·y, so that the observed capacity loss is four times higher than the loss that would be simply expected by the blocking of free Li sites by inactive Ni. The authors confirmed a strong polarization effect originating from slowed Li diffusion kinetics. This generalized $C/C_0 = f(y)$ correlation can be used to estimate the impact of a maximum of 2% increase in Ni_{Li} over 700 cycles (see Fig. 3b) on the capacity, since y equals approximately v_{Ni} in the structural model of NCM-811 (please note that $Ni_{Li} = v_{Ni} \cdot 100\%$). For a maximum increase of Ni_{Li} by 2% from BOT to EOT, the capacity fading predicted by the above relationship observed by Makimura et al. would amount to 8% or ≈18 mAh g^{-1} (based on an initial capacity of ≈221 mAh g^{-1} at C/10, see Fig. 1a). This is ≈45% of the overall capacity loss of ≈40 mAh g^{-1} at C/10 (same C-rate as applied by Makimura et al.[47]). It is difficult to make any statement about the Li diffusion kinetics of NCM-811. The cathode mean charge voltage could be fully explained by the increase of R_{DCIR} at ≈4.0 V (see Table II), which in turn is a direct measure of R_{CT} (see Fig. 2), but $\tilde{D}_{Li}$ might potentially have an impact on the more pronounced change of the cathode mean discharge voltage. In this context, Makimura et al. observed a higher polarization during discharge than during charge with increasing y, but at the same time the capacity was more limited in the charge than discharge endpoint (ratio of ≈2/1).[47] In summary, the cycling-induced increase of the Li-Ni mixing by ≈1%–2% over 700 cycles might appear negligible, but its contribution to the capacity fading due to the slowed Li diffusion kinetics in the bulk phase could indeed be relevant. Since the correlation reported for NCA samples by Makimura et al. might not be fully applicable to our NCM-811 CAM, however, the precise quantification of the capacity loss caused by increasing Li–Ni mixing remains elusive.

Finally, we want to look at a recent study of Li et al., where NCM-811 was cycled for 1000 cycles at 25 °C to different upper cut-off voltages in NCM-811/graphite full-cells.[44] For cycling until 4.2 and 4.4 V_{FC}, which translates into ≈4.3 and ≈4.5 V vs Li^+/Li, the authors report the Li-Ni mixing to increase vastly by 6.7% and 11.9%, respectively. Unfortunately, their structural model is barely described in the publication, which makes it difficult to compare their results to ours. According to the $C/C_0 = f(y)$ correlation by Makimura et al.,[47] the Li-Ni mixing has to account completely (and beyond) for the observed capacity fading (78% and 52% capacity retention). This refinement result seems to be quite unlikely, because Li et al. also identified other important degradation mechanisms such as TM dissolution and deposition on the anode, surface NiO formation, and particle cracking.[44]

Lithium content via XPD analysis.—The above evaluation of the XPD data from the cathodes harvested in the discharged state already indicated a steady decrease of the lithium content of the discharged NCM-811 CAM upon cycling (see x_{Li} in Table III). This behavior can be easily rationalized by the increasing overpotential (e.g., reflected by the changes in the mean charge/discharge cathode voltage, see Fig. 1b), which narrows the accessible SOC window from both sides in the completely discharged and charged states when cycling the NCM-811 electrode in the fixed cathode voltage window of 3.0–4.5 V. In our study conducted at 22 °C,[9] the x_{Li} data from in situ XPD were the centerpiece to deconvolute the capacity loss into its contributions originating from the increase of R_{CT} related overpotentials and from a loss of cyclable cathode active material. This analysis shall also be applied here based on ex situ XPD data. Since the full-cells were stopped during C/2 cycling after running into the lower cut-off voltage, XPD data in the discharged state of the harvested NCM-811 cathodes could be acquired immediately. For XPD analysis in the charged state, we punched out smaller electrodes, which were cycled in half-cells at C/2 for 1.5 more cycles and which were then disassembled after running into the upper cut-off cathode voltage of 4.5 V. The *c/a* lattice parameter ratio from the diffractograms and the thereof determined lithium content are summarized in Fig. 4.

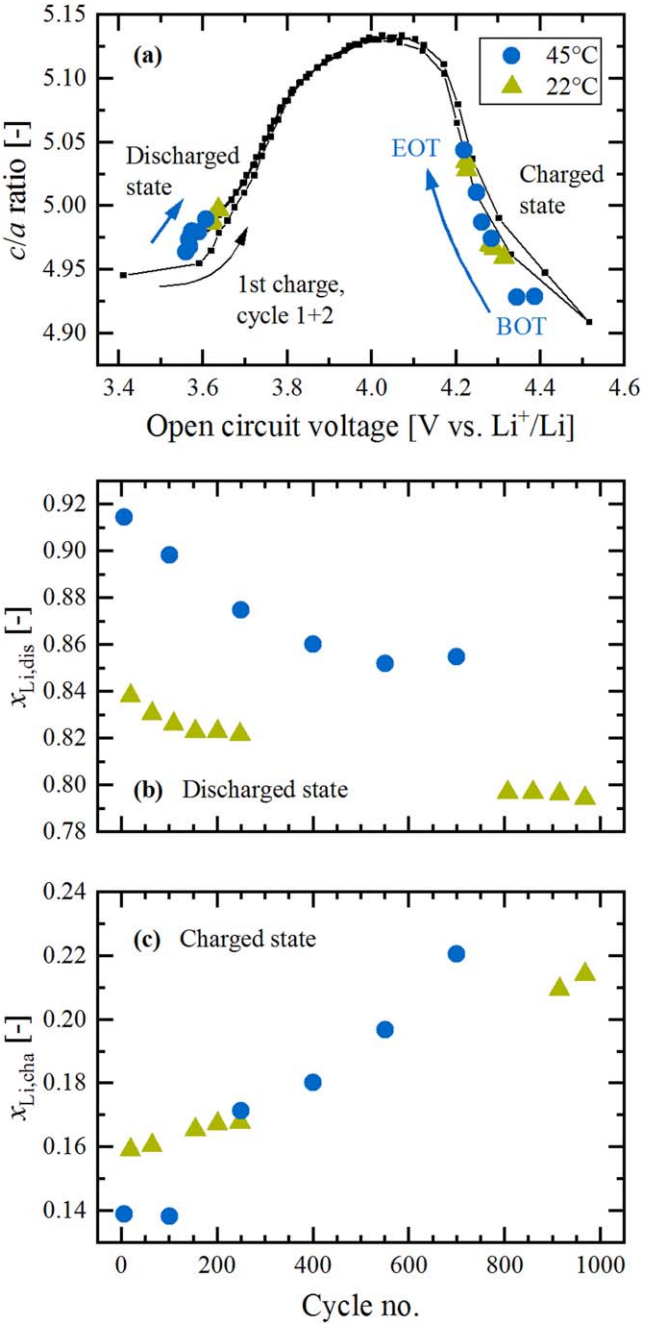

Figure 4. Determination of the lithium content in the discharged and charged state of NCM-811 electrodes operated between cathode potentials of 3.0–4.5 V at C/2 and different cycling temperatures. (a) Evolution of the underlying c/a lattice parameter ratio vs OCV and comparison to the c/a curve of a fresh NCM-811 cathode in cycle 1 and 2 (black squares/lines). The cycle 1 + 2 curve and the in situ XPD data for cycling at 22 °C (green triangles) were taken from our previous publication (see curves labeled "Cycle 1 + 2" and "LDE, cell 1" in Fig. 6a of Friedrich et al.,[9] published by ECS, licensed as CC BY 4.0). The ex situ XPD data at 45 °C (blue circles) originate directly from the harvested full-cell electrodes (discharged state) or from harvested electrodes that were subjected to another 1.5 half-cell cycles (charged state) and are shown vs the final OCV value at 25 °C (see Experimental section). The c/a data points are converted into the lithium content: (b) in the discharged state via Eq. 2, referred to as $x_{Li,dis}$; (c) in the charged state via Eq. 3, referred to as $x_{Li,cha}$. At 45 °C, the BOT value of $x_{Li,dis} \approx 0.915$ slightly exceeds the margin of the c/a calibration curve, but additional ex situ points of fresh NCM-811 cathodes showed that Eq. 2 holds true until ≈0.95.

The $x_{Li} = f(c/a)$ calibration curves were measured within the first cycles of a fresh NCM-811 cathode,[9] where the lithium content (x_{Li}) can be deduced fairly accurately from the exchanged capacity (assuming purely faradaic currents from lithium de-/intercalation into the CAM). This approximation is not true anymore during prolonged cycling, due to the charge accumulation caused by tiny parasitic currents. Consequently, it is difficult to prove if the initially determined calibration curves and the extracted x_{Li} values are still valid, because there is no direct measure of the CAM's state of charge. On the other side, we continuously tracked the open circuit voltage (at 45 °C and finally also at 25 °C), and the *c*/*a* ratio is shown as a function of the OCV at 25 °C in Fig. 4a. Here, the *c*/*a* data from 45 °C cycling (blue circles in Fig. 4a) are contrasted with the data from 22 °C cycling (green triangles) and with the full $c/a = f(OCV)$ curve of a fresh NCM-811 cathode (black squares/lines). Note that the OCV values are known for every measurement, i.e., all datasets can be compared with each other without any correction. We see that, independent of the cycling temperature, the *c*/*a* data in the completely discharged and charged state coincide nicely with the initial calibration curve. The *c*/*a* values increase with cycling in both the discharged and charged state, indicating a shrinking OCV window. Since the $c/a = f(OCV)$ correlation is maintained upon cycling and since the OCV is an indirect measure of the absolute SOC (i.e., the SOC referenced to x_{Li}), we can continue to convert the *c*/*a* ratio into the lithium content. This is done by applying Eq. 2 for the discharged state (see $x_{Li,dis}$ in Fig. 4b) and by applying Eq. 3 for the charged state (see $x_{Li,cha}$ in Fig. 4c), respectively. For a more detailed explanation of this procedure see the Experimental section and Friedrich et al.[9]

Let us first look at the BOT values, where the 45 °C capacity is ≈24 mAh g^{-1} higher than at 22 °C (see Table I). This capacity gain predominantly occurs in the discharged state, because $x_{Li,dis}$ is higher by ≈0.08 in the discharged state (see Fig. 4b), while $x_{Li,cha}$ is only lower by ≈0.02 in the charged state (see Fig. 4c), corresponding to a ratio in Δx_{Li} of ≈4/1. Based on d*Q*/d*V* plots, Li et al. also reported that the low-SOC capacity (i.e., towards the discharged state) of NCA depends strongly on temperature (and mildly on C-rate), but the high-SOC limit (i.e., towards the charged state) is hardly affected by neither temperature nor C-rate.[13] They explain this behavior by the kinetic hindrance from solid-state lithium diffusion, which hampers the lithium intercalation back into the layered oxide during discharge. In the following, $x_{Li,dis}$ continuously decreases while $x_{Li,cha}$ increases with cycling, as already anticipated from the $c/a = f$ (OCV) raw data (see Fig. 4a). The changes are quite uniform, except for the $x_{Li,cha}$ value after 100 cycles at 45 °C that remains at the value of ≈0.14 obtained after 6 cycles (see Fig. 4c). Furthermore, $x_{Li,dis}$ does not continue to decrease anymore between 550 and 700 cycles (see Fig. 4b). Comparing the changes in x_{Li} from BOT to EOT between both temperatures, $\Delta x_{Li,dis}$ and $\Delta x_{Li,cha}$ are by a factor of ≈1.4–1.5 higher after 700 cycles at 45 °C compared to 1000 cycles at 22 °C ($|\Delta x_{Li,dis}|$: ≈0.044 at 22 °C vs ≈0.060 at 45 °C; $\Delta x_{Li,cha}$: ≈0.055 at 22 °C vs ≈0.081 at 45 °C). This result is in line with the more strongly increasing overpotential at the higher temperature, as outlined in the previous paragraphs. However, it is difficult to relate the Δx_{Li} differences quantitatively to the mean cathode voltages (Fig. 1b) or to the R_{DCIR}/R_{CT} evolution (Fig. 2b), because only the resistances in the low- and high-SOC region towards the voltage cut-offs matter for the overpotential-induced capacity loss (but these resistances are not directly addressed by the former measures).

In light of the results from Figs. 3 and 4, we want to emphasize that the aged NCM-811 CAM could be always refined as a single phase based on the Rietveld refinement of the ex situ XPD data. This is in contrast to some operando studies about Ni-rich NCMs and NCAs (with 80%–85%$_{Ni}$), which detected the emergence of two to three simultaneously present layered phases over the course of long-term cycling, especially in the charged (delithiated) state.[15,45,48,49] Xu et al. observed a so-called "fatigued" phase of NCM-811 (together with an "active" and "intermediate" phase), whose upper SOC limit was fixed at approximately 75% (corresponding to $x_{Li,cha} \approx 0.25$).[45] They assign this threshold to the increasing interfacial lattice strain between the reconstructed rock-salt surface layer (caused by lattice oxygen release at high SOCs) and the bulk layered structure beyond ≈75% SOC. The segregation into several phases might however disappear in the charged state when the CAM is held long enough under constant voltage[15] or open circuit voltage.[49] Despite forming a reconstructed surface layer, we could operate NCM-811 continuously to $x_{Li,cha}$ values below 0.25 (see Fig. 4c) without any evidence for an additional "fatigued" layered phase in the XPD data, contrary to the up to ≈70% observed by Xu et al.[45] This is perhaps due to the observation that such a fatigued phase may only occur upon extensive particle cracking, in which case Schweidler et al. observed the occurrence of a fatigued phase that nevertheless could be fully accessed at very low currents.[15]

Capacity loss analysis.—With the XPD-derived x_{Li} data, we can now proceed to perform the capacity loss analysis. Here, the material loss is probably the most interesting parameter, which quantifies the fraction of the electrochemically active CAM lost and/or converted into an electrochemically inactive phase upon cycling. In the former 22 °C study, the material loss could be explained by the formation of a resistive, oxygen-deficient surface layer around the primary particles, and this loss of electrochemically active material was calculated in percentage terms relative to the pristine CAM as follows:[9]

$$\Delta C^{i}_{Material,rel} = \frac{C^{i}_{XPD} - C^{i}_{EC}}{C^{i}_{XPD}} \quad [5]$$

where C^{i}_{EC} (in mAh g^{-1}) is the electrochemically measured discharge capacity in the ith cycle and C^{i}_{XPD} (also in mAh g^{-1}) is the theoretically expected capacity inferred from XPD:

$$C^{i}_{XPD} = (x^{i}_{Li,dis} - x^{i}_{Li,cha}) \cdot \frac{274\ \text{mAh g}^{-1}}{1.01} \quad [6]$$

C^{i}_{XPD} is applied to the whole CAM and thus assumes no material to be lost while aging, but it considers the narrowed SOC window during C/2 cycling due to the actually present overpotential in the ith cycle. Thus, the difference between C^{i}_{XPD} and C^{i}_{EC} represents the loss of electrochemically active material in the ith cycle (in mAh g^{-1}); if this difference is normalized by C^{i}_{XPD}, it reflects the relative loss of electrochemically active material. Please note that 274 mAh g^{-1} correspond to the theoretical capacity for complete lithium extraction of 1.01 from the pristine CAM (see Experimental section).

Even though providing quantitative insights into CAM degradation, we admit that the XPD analysis is not really practical to be applied on a routine basis, since it requires a precise $x_{Li} = f(c/a)$ calibration curve for every CAM and that the bulk of the CAM stays fairly unaltered under the testing conditions (e.g., extensive Li-Ni mixing[44] or lattice dislocations[50] could potentially modify the $x_{Li} = f(c/a)$ relationship). These drawbacks call for alternative methods. Relying solely on electrochemical data, Dahn's group developed a differential voltage analysis software (which also requires that the bulk of the CAM does not change upon cycling).[51] Here, d*V*/d*Q* vs *Q* curves of the cycled full-cell are compared to reference half-cells from anode and cathode. They are matched with each other by adjusting two parameters for each electrode: the electrochemically active mass of the electrodes and their capacity slippage. Other diagnostic and prognostic tools use a similar set of parameters to model battery aging from experimental data.[52,53] The loss of electrochemically active material can then be calculated from the decrease of the cathode mass.

In our previous publication, we also tried to estimate the material loss by applying a C-rate test and comparing the electrochemical

capacity in the ith cycle (C^{i}_{EC}) to an adequate reference state (C^{0}_{EC}):

$$\Delta C^{i}_{Material,rel} = \frac{C^{0}_{EC} - C^{i}_{EC}}{C^{0}_{EC}} \quad [7]$$

There are two important requirements to be fulfilled by the reference state: (i) it must not yet have experienced an electrochemically active material loss, which limits the reference state to the initial cycles; and, (ii) the overpotential must be negligible, which demands that C^{0}_{EC} and C^{i}_{EC} are measured at a very slow C-rate. Under these conditions, any reversible capacity loss can be compensated for and only the irreversible loss of electrochemically active material remains. In our previous work with the same NCM-811 CAM, it turned out that a C-rate of C/50 was sufficiently slow to minimize the impact of overpotentials on the attained capacity.[9] C/50 cycling at 45 °C between cathode potentials of 3.0–4.5 V delivers a discharge capacity of $C^{0}_{EC} = 228 \pm 1$ mAh g^{-1} within the first two cycles of a pristine NCM-811 cathode (which is quite close to the 221 ± 1 mAh g^{-1} obtained a C/10, see Fig. 1a). Electrodes that were punched out from the cathodes harvested from the cycled pouch cells were also subjected to two C/50 cycles (following EIS at C/10, see Experimental section). The cathode mean discharge voltage of the cycled electrodes agrees within less than 35 mV (lower) with that of the pristine cathode, even though the mean discharge voltage after 700 cycles has decreased by ≈80 mV at C/10 and ≈250 mV at C/2 (see Fig. 1b). This implies that the resistance increase over cycling does not result in any significant overpotential at this very low C-rate of C/50, i.e., the above requirements for this analysis are satisfied.

Figure 5 compares the relative material loss of the electrodes cycled at 45 °C and calculated by this EC method (black squares, acc. to Eq. 7) to that calculated by the XPD analysis (acc. to Eq. 5) for the electrodes cycled at 45 °C (blue circles) and those cycled at 22 °C in our previous study (green triangles). Focusing first on the electrodes cycled at 45 °C, Fig. 5 shows that the electrochemically active material loss obtained by the EC vs the XPD method, both independent datasets, match extremely well within ±1 percentage points. The only exception is the EOT sample after 700 cycles, where the XPD-derived material loss (≈18.2%) exceeds that obtained from the EC method (≈15.6%) by ≈2.6 percentage points. This difference could potentially be explained by a slightly too high $x_{Li,dis}$ value (see Fig. 4b), which in turn would increase C^{i}_{XPD} and thus the XPD-based $\Delta C^{i}_{Material,rel}$ value (see Eqs. 5 and 6).

For the electrodes cycled at 22 °C, most of the electrochemically active material get lost within the first 200–300 cycles, then leveling off and reaching ≈8.5% after 1000 cycles. For the electrodes cycled at 45 °C, the progress of the material loss shows a similar trend in the beginning, but contrary to the 22 °C data, it does not diminish until 700 cycles. Even though the trend is not exactly clear, either possessing a sharp rise from 550 to 700 cycles (as indicated by the XPD method) or a more uniform increase (as suggested by the EC method), the EOT value after 700 cycles at 45 °C amounts to ≈15.6%–18.2% and is thus twice as big than after 1000 cycles at 22 °C. Using the dV/dQ analysis software,[51] Li et al. tracked the CAM loss of their NCA/graphite full-cells cycled at 40 °C.[13] For the upper cut-off voltage of 4.3 V_{FC} (corresponding to ≈4.4 V vs Li^{+}/Li), the calculated CAM loss amounts to 4.3 ± 0.5% and 10.1 ± 0.5% after 400 and 800 cycles, respectively. While these losses for NCA are ≈2-fold lower than those in this study for NCM-811, this may not only be due to the different active materials but also due to the here used ≈0.1 V higher upper cathode potential and the 5 °C higher temperature. In an earlier publication from the Dahn group, they reported ≈8% of lost NCM-811 after only 83 cycles under very similar conditions (again 40 °C and 4.3 V_{FC}),[54] which seems quite large compared to our data. All these datasets point towards the influence of the cycling conditions (e.g., temperature, upper cut-off voltage, and depth of discharge) and the nature of the CAM (e.g., NCM vs NCA) on the extent of material loss, so that a quantitative comparison with other work in the literature is typically not possible.

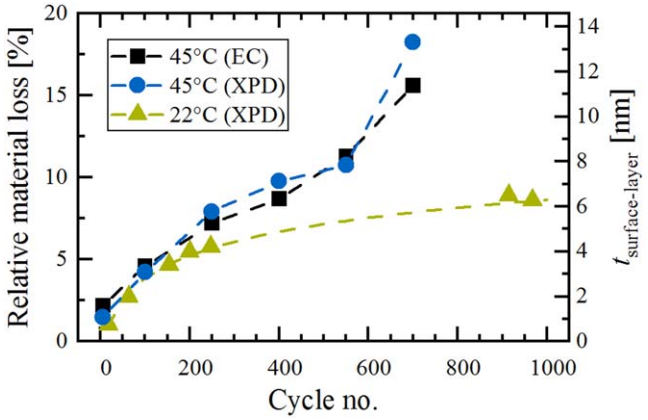

Figure 5. Determination of the NCM-811 material loss ($\Delta C^{i}_{Material,rel}$) upon extended cycling at 45 °C between cathode potentials of 3.0–4.5 V, either determined from slow C/50 cycling of the harvested cathodes (EC method using Eq. 7; black squares), or from our XPD analysis (using Eqs. 5 and 6; blue circles). The XPD data at 22 °C (green triangles) were taken from our previous publication (see data labeled "Cell 1" in Fig. 5c of Friedrich et al.,[9] published by ECS, licensed as CC BY 4.0). The material loss in percentage terms is converted into the thickness of a resistive, O-depleted surface layer on the right. Here, we assumed spherical primary particles, whose average diameter of ≈410 nm was estimated from the BET surface area of a charged electrode (≈3.1 m^2/g_{CAM}, see later discussion); for details of this calculation see the supporting information of Ref. 9.

But what causes the temperature dependence in this work? The more pronounced material loss at elevated temperature suggests a thicker reconstructed, oxygen-depleted surface layer. However, the upper SOC limit is almost not affected by the temperature rise, as was already seen for the BOT values of $x_{Li,cha}$ at C/2 (see Fig. 4c) as well as for the C/10 formation cycles (absolute SOC values of ≈85% vs ≈86%). Since the oxygen release that leads to the surface transformation predominantly depends on the maximum SOC (i.e., the extent of delithiation),[32,33] one would expect a similar driving force for oxygen release for the cycling conditions at both temperatures. On the other hand, the kinetics of the surface reconstruction would be expected to be faster (e.g., for oxygen transport and TM rearrangement), by which the O-depleted, spinel/rock-salt-like layer would be able to penetrate deeper into the primary particles. The temperature dependence of the initial oxygen release was studied by Jung et al. for an NCM-622 CAM.[14] Taking the sum of evolved O_2, CO, and CO_2 within the first four cycles until 4.8 V_{FC}, the gassing caused by oxygen release increased by a factor of ≈1.5 and ≈1.9 when increasing the temperature from 25 °C to 40 °C or to 50 °C, respectively. In our case, the NCM-811 CAM operates for most of the time above the SOC threshold for oxygen release at ≈80%, corresponding to an $x_{Li,cha}$ value of ≈0.20 at the upper cut-off potential. As shown in Fig. 4c, $x_{Li,cha}$ remains below 0.20 for the first ≈750 cycles during 22 °C operation (interpolated from a linear fit through the existing data) and for ≈550 cycles during 45 °C operation. Consequently, the oxygen release could proceed almost unlimited; however, Jung et al. further showed that the oxygen release diminishes from cycle to cycle.[14] At 40 °C, e.g., the gassing of the NCM-622 CAM in cycle 2–4 reduced by a factor of ≈2.2, ≈3.7, and ≈4.0 compared to the first cycle. Even though we cannot finally say for how long oxygen is released from the CAM surface, we want to emphasize that the here quantified fraction of lost CAM does not directly correspond to the accumulated amount of evolved lattice oxygen until the respective cycle number. The transformation of the electrochemically active, layered structure into an electrochemically inactive, resistive surface layer is assumed to be a two-step process.[9] After the initial oxygen release, the

Table IV. Deconvolution of the electrochemically measured capacity loss from BOT to EOT ($\Delta C_{EC}^{BOT\rightarrow EOT}$) into its contributions originating from the loss of cyclable CAM ($\Delta C_{Material}^{BOT\rightarrow EOT}$) and the overpotential-induced loss ($\Delta C_{Overpotential}^{BOT\rightarrow EOT}$). $\Delta C_{Overpotential}^{BOT\rightarrow EOT}$ can be further divided into capacity losses in the discharged ($\Delta C_{Discharge}^{BOT\rightarrow EOT}$) and charged state ($\Delta C_{Charge}^{BOT\rightarrow EOT}$), respectively. The underlying equations of the XPD analysis are provided in the Appendix and the values at ambient temperature stem from our previous publication of the same material.[9] The sum of $\Delta C_{Material}^{BOT\rightarrow EOT}$ and $\Delta C_{Overpotential}^{BOT\rightarrow EOT}$ exceeds $\Delta C_{EC}^{BOT\rightarrow EOT}$ due to rounding errors and due to the fact that some material loss was already acquired until BOT.

C/2 capacity loss [mAh g^{-1}]	Equation	Ambient temperature (22 °C)	Elevated temperature (45 °C)
BOT → EOT		Cycle 18 → 1000	Cycle 6 → 700
$\Delta C_{EC}^{BOT\rightarrow EOT}$	(A·1)	≈38	≈68
$\Delta C_{Material}^{BOT\rightarrow EOT}$	(A·2)	≈16	≈40
$\Delta C_{Overpotential}^{BOT\rightarrow EOT}$	(A·3)	≈25	≈31
- $\Delta C_{Discharge}^{BOT\rightarrow EOT}$	(A·4)	≈11	≈13
- $\Delta C_{Charge}^{BOT\rightarrow EOT}$	(A·5)	≈14	≈18

transition-metals in the then O-depleted structure have to rearrange to form a spinel/rock-salt-type surface layer, which is incapable of reversibly de-/intercalating a significant amount of lithium-ions. While both steps run basically in parallel during the thermal decomposition of charged NCM/NCA CAMs,[5,55] the TM rearrangement is expected to be retarded during electrochemical cycling. For Li-rich NCMs at 25 °C, HR-TEM images have shown that the actual reconstruction happens within 20–50 cycles.[56] As vacancies in the TM layer probably facilitate the rearrangement in Li-rich NCMs, it is reasonable to assume that this process takes longer for regular NCMs (here >100 cycles).

Using the set of XPD-based equations introduced in our former study,[9] which are shortly summarized in the Appendix of this work, Table IV deconvolutes the BOT-to-EOT capacity losses measured at 22 °C and 45 °C. Here, the electrochemically measured capacity losses at C/2 ($\Delta C_{EC}^{BOT\rightarrow EOT}$, see Eq. A·1) amount to ≈38 mAh g^{-1} for cycling at 22 °C (cycles 18 to 1000) and to ≈68 mAh g^{-1} for cycling at 45 °C (cycles 6 to 700; see also Table I). As already anticipated by the relative material losses in Fig. 5, this difference of ≈30 mAh g^{-1} is largely dominated by the extent of surface reconstruction at ambient vs elevated temperature, which translates into absolute capacity losses ($\Delta C_{Material}^{BOT\rightarrow EOT}$, see Eq. A·2) of ≈16 mAh g^{-1} for cycling at 22 °C and ≈40 mAh g^{-1} for cycling at 45 °C, respectively. This is a ≈2.5-fold increase caused by the enhanced loss of cyclable NCM-811 CAM when increasing the cycling temperature. On the other hand, the overpotential-induced capacity loss ($\Delta C_{Overpotential}^{BOT\rightarrow EOT}$, see Eq. A·3) increases only by factor of ≈1.2 (from ≈25 mAh g^{-1} at 22 °C to ≈31 mAh g^{-1} at 45 °C), which is composed of contributions from the discharged state ($\Delta C_{Discharge}^{BOT\rightarrow EOT}$, see Eq. A·4) and from the charged state ($\Delta C_{Charge}^{BOT\rightarrow EOT}$, see A·5). At the first glance, this moderate rise of the overpotential-related losses is less than that projected from the underlying x_{Li} data: $\Delta x_{Li,dis}^{BOT\rightarrow EOT}$ (see Fig. 4b) and $\Delta x_{Li,cha}^{BOT\rightarrow EOT}$ (see Fig. 4c) increase by a factor of ≈1.4–1.5 when increasing the cycling temperature from 22 to 45 °C. This discrepancy is due to the fact that $\Delta C_{Overpotential}^{BOT\rightarrow EOT}$ (and its individual components in the discharged and charged state) have to be corrected by the phase fraction of lost NCM-811 CAM, because only the cyclable CAM can experience a capacity loss due to an increasing overpotential. Consequently, as the relative material loss is doubled after 700 cycles at 45 °C compared to 1000 cycles at 22 °C (see Fig. 5), the overpotential-induced capacity losses in units of mAh g^{-1} turn out to be smaller than the shrinkage of the accessible Δx_{Li} window of the retained NCM-811 CAM.

Cracking and surface layer thickness.—Finally, we want to estimate the thickness of the reconstructed surface layer formed over extended cycling. This question requires to determine the surface area of the CAM, which will change upon cycling due to particle cracking.[9,25] Figure 6 shows the evolution of the specific NCM-811 surface area of the cycled electrodes harvested in the discharged state (black data points), as determined by Kr-BET measurements. Here, the contribution of the NCM-811 CAM was calculated according to Eq. 4 by subtracting the share of the electrode additives (2 wt% SFG6L graphite, 1 wt% C65 carbon black, and 3 wt% PVDF binder) in the composite cathode. Their surface area was determined from additives-only electrodes, consisting only of the inert components with the same weight ratio as in the actual cathodes, yielding $A_{BET,add}$ = 5.10 m^2/g_{add} for fresh and 5.56 m^2/g_{add} for cycled additives-only electrodes (see Experimental section). This approach assumes that the binder does not significantly alter the accessible surface area of the CAM in the cathode electrodes, even though the binder was found to reduce the surface area of the conductive agents by a factor of ≈3 in the additives-only electrodes (see Experimental section). To prove this assumption, we can compare the surface area of the pristine NCM-811 CAM in its form as pure powder of 0.28 m^2/g_{CAM} (blue line in Fig. 6) with that obtained for the CAM in the fresh cathode electrode of 0.30 ± 0.02 m^2/g_{CAM} (determined from the electrode specific surface area of $A_{BET,elec}$ = 0.58 ± 0.01 m^2/g_{elec} by subtracting the weight-fraction-normalized value of $A_{BET,add}$ acc. to Eq. 4; average from two measurements). Since the CAM specific

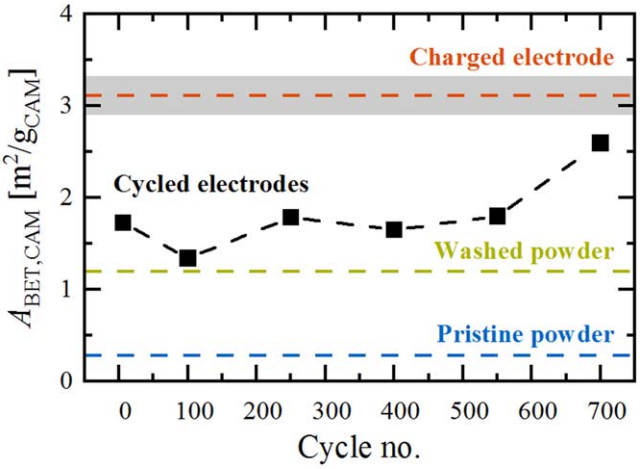

Figure 6. Evolution of the NCM-811 surface area ($A_{BET,CAM}$) during long-term cycling at 45 °C. The cycled electrodes (black data points) were measured in the discharged state by Kr-BET (following the rate test and washing steps with aprotic solvents; see Experimental section), whereby the surface area contribution of the CAM was calculated according to Eq. 4. In order to provide some reference points (depicted as horizontal lines), the $A_{BET,CAM}$ values of the cycled electrodes are compared to those of the pristine NCM-811 powder (blue line), of washed NCM-811 powder (either in water or HF-containing electrolyte; green line), and of a charged electrode (after a first charge at C/10 to a cathode potential of 4.5 V at 45 °C; red line).

surface areas of the pristine NCM-811 powder and cathode electrode agree nicely with each other, we can now continue with the surface area analysis of the cycled electrodes (black data points in Fig. 6).

In the cycled electrodes, the surface area of the NCM-811 CAM is on a rather constant level of ≈1.8 m^2/g_{CAM} and only increases to ≈2.6 m^2/g_{CAM} at the end-of-test after 700 cycles. To evaluate these numbers, some important reference points are shown as horizontal lines in Fig. 6. The afore-mentioned pristine CAM powder (blue line) has a significantly lower surface area of 0.28 m^2/g_{CAM}. Assuming solid spheres and using the crystallographic density of 4.75 g cm^{-3}, this value translates into an average particle diameter of $d_{avg} \approx 4.5$ μm ($d_{avg} = 6/(\rho_{cryst} \cdot A_{BET,CAM})$), which is on the order of the secondary agglomerates (d_{50} value of 10.2 μm determined by laser scattering). Consequently, we predominantly see the outer surface of the secondary agglomerates, while the inner surface of the primary particles is not accessible for two reasons: (i) the crystallites are closely packed after calcination with little pore volume in between and (ii) the pore space between the primary crystallites is blocked due to the presence of surface impurities such Li_2CO_3 and LiOH. As shown in our first publication for the same NCM-811 CAM,[9] these impurities can be removed by washing the CAM powder in water or by storing it in an HF-containing electrolyte, yielding in both cases 1.2 m^2/g_{CAM} (green line). The surface area of the cycled electrodes is still higher (≈1.3–2.6 m^2/g_{CAM}; see black squares in Fig. 6), because the crystallites experience a continuous contraction/expansion during charge/discharge cycling. Under the given conditions (C/2 cycling at 45 °C between cathode potentials of 3.0–4.5 V), the change of the unit cell volume, $\Delta V/V_{dis}$, evolves from −6.1% at BOT to −3.1% at EOT. Since the unit cell volume shrinks predominantly at high SOCs ($x_{Li} < 0.35$ for NCM materials),[57] $\Delta V/V_{dis}$ gets smaller over the course of cycling due to the gradual increase of $x_{Li,cha}$ at the upper cut-off voltage (see Fig. 4c). The reversible "breathing" in every single cycle accumulates a mismatch between the primary particles, so that their packing in the discharged state is not as dense as it was in the pristine state, exposing additional inner surface area.

When we develop this argument further, the contracted crystallites in the charged state should exhibit the highest surface area. For this reason, we also measured Kr-BET of the charged electrodes after the first charge at C/10 to a cathode potential of 4.5 V at 45 °C, yielding a specific surface area of the CAM of 3.1 ± 0.2 m^2/g_{CAM} (average from two electrodes; red line). For solid spheres, this gives an average diameter of $d_{avg} \approx 0.41 \pm 0.03$ μm, which indeed reflects the size of the primary particles (see Fig. S11 -in our former study[9]). Oswald et al. have visualized these alternating phenomena by cross-sectional FIB-SEM images of NCM-622, illustrating (i) the separation of primary particles in the charged state and (ii) their subsequent compaction in the discharged state.[25] After 303 cycles to a cathode potential of 4.5 V at 25 °C, they reported a surface area of ≈3.1 m^2/g_{CAM} in the discharged state, which resembles that of our NCM-811 CAM in the charged state of the first cycle.

Alternatively, Oswald et al. introduced an EIS-based method to monitor the surface area of electrodes by utilizing its correlation to the electrochemical double layer capacitance.[25] Kr-BET and EIS have some intrinsic differences. Most importantly, krypton atoms can access pores as small as ≈0.2 nm, while the penetration of solvated lithium-ions into pores requires pore diameters of greater than ≈1 nm, so that only pores above this value will contribute to the capacitance determined by EIS. This might explain why the here reported surface area changes determined by Kr-BET (see Fig. 6) occur mainly from the pristine state to BOT (6 cycles): after the initial few cycles, the surface impurities seem to be already removed and the particle disintegration seems to have already created permanent pores at least on the sub-nm scale, which can be detected right away by Kr-BET. In Oswald's EIS data, there is also a sharp but less extensive rise in the first cycles and the capacitance increases notably in the later cycles as well. This is rationalized by the steady expansion of pores (or cracks) in the discharged state (due to the accumulating mismatch between the primary crystallites), so that the further increase of CAM surface area only becomes detectable by EIS after a certain pore/crack size threshold has been reached.

The above discussion highlights the coexistence of solid/solid, solid/liquid, and solid/gas interfaces within the secondary agglomerates. As their relative ratio will change during cycling, we have to select a proper surface area for the calculation of the surface layer thickness. In this respect, recent publications address the question if the surface reconstruction requires the exposure of the surface to the electrolyte.[15,58,59] In the work of Schweidler et al.[15] and Zou et al.,[58] STEM imaging of cycled Ni-rich CAMs revealed reconstruction layers on open surfaces (exposed to the electrolyte), while the layered structure was maintained on sealed surfaces (not in contact with the electrolyte). For solid/solid interfaces, Zou et al. further differentiate between incoherent boundaries (stable against phase transitions) and twin boundaries (prone to phase transitions). All these different modes of surface reconstruction can be ascribed to intergranular cracking. In contrast, Ahmed et al. reported on the growth of rock-salt-like regions at the boundary of intragranular nanopores, which are encapsulated in the bulk of the CAM and thus not exposed to the electrolyte.[59] Yan et al. identified intragranular cracks, which are initiated from the grain interior and can generate completely new surfaces (in contrast to sealed surfaces, which are already present, but buried).[50] We conclude that the surface reconstruction depends on the type of grain boundary and its exposure to the electrolyte. Consequently, the calculated thickness can just provide an estimate, which averages over the heterogeneous surfaces. We decided to proceed with the ≈3.1 m^2/g_{CAM} of the charged electrode, because this value represents in good approximation all available surfaces of the crystallites, which might potentially be exposed to the electrolyte (due to intergranular cracking, particularly in the charged state). Furthermore, the layered-to-spinel/rock-salt transformation is initiated by the release of lattice oxygen at these high SOCs.

Using the equations described in our former work,[9] the relative material loss (left axis in Fig. 5) is converted into the average thickness, $t_{surface\text{-}layer}$ (right axis in Fig. 5). As already discussed beforehand, we want to mention that the here calculated thickness represents the electrochemically inactive surface layer, which yet might be thinner than the O-depleted surface layer at a given cycle number. The initial oxygen release has to be completed by the rearrangement of the transition-metals in order to be become detectable as lost CAM. Therefore, we assume several reaction fronts, which gradually grow from the surface of the primary particles into their interior, but only the fully reconstructed and non-intercalating layer can be measured by our approach. With the ≈3.1 m^2/g_{CAM} of the charged electrode, the re-calculation of the EOT value after 1000 cycles at 22 °C now gives ≈6 nm, which agrees much better to the HAADF-STEM images in our previous study than the back then estimated ≈15 nm on the basis of the 1.2 m^2/g_{CAM} of the washed CAM. At 45 °C, the surface layer thickness amounts to ≈12–14 nm after 700 cycles. Even though all quantification methods, either XPD and Kr-BET (as applied here) or STEM imaging, should be taken with a grain of salt, the 45 °C trend line is in good agreement to the STEM data of Schweidler et al.[15] Similar to our NCM-811, they cycled their NCM-851005 at 45 °C to 4.2 V_{FC} (corresponding to ≈4.3 V vs Li^+/Li) and reported a rock-salt-like phase of ≈2 nm after 100 cycles and ≈14 nm after 500 cycles, respectively. In light of the above arguments, the observed surface layer is however not perfectly uniform around the individual primary particles.[15] Consequently, the average thickness of ≈14 nm after 500 cycles reported by Schweidler et al.[15] is in a reasonably good agreement with the here estimated ≈8 nm for the NCM-811 electrode cycled for 550 cycles (see Fig. 5). In summary, the CAM surface area and the thickness of the reconstruction layer can be accessed by various methods, including microscopy, BET, and EIS. In order to evaluate how quantitative their agreement can be in the best case, all these methods have to be applied to the same material in a complementary manner.

Our data as well as all the discussed data and findings from other groups are based on poly-crystalline CAMs, but there is an ongoing trend to switch to single-crystalline layered oxides.[16,60–62] In that case, the crystallites have a size in the μm range. As long as intragranular cracking of individual crystallites does not generate new surfaces, e.g., due to real particle fracture, we would expect the surface area of single-crystalline CAMs to stay below 1 m^2/g_{CAM} also during cycling. The lower surface-to-bulk ratio would substantially decrease the loss of electrochemically active material (assuming that it is occurring mostly on CAM surfaces exposed to the electrolyte) and the associated degradation mechanism. This is an interesting working hypothesis for single-crystalline CAMs to look at in the future.

Conclusions

In the present work, we investigated in a comparative manner the degradation mechanisms of the Ni-rich layered oxide NCM-811 at ambient (22 °C) and elevated temperatures (45 °C). Apart from the temperature variation, the NCM-811/graphite full-cells were cycled in a very similar fashion at a constant-current of C/2 between cathode potentials of 3.0 and 4.5 V. In order to focus solely on the CAM degradation and to exclude any effects due to a lithium loss at the anode, the graphite CE was partially pre-lithiated and the potential was controlled vs the Li-RE. Furthermore, the large electrolyte excess prevents any capacity fading caused by the potential electrolyte breakdown.

The capacity loss during C/2 cycling was more than doubled at 45 °C operation (data generated in this work) compared to 22 °C operation (data acquired in our first study[9]). To elucidate the underlying degradation mechanisms, we switched from time-consuming in situ techniques to their simplified ex situ counterparts, including X-ray powder diffraction, electrochemical impedance spectroscopy, and Kr-BET. We could ascribe ≈60% of the observed capacity loss after 700 cycles at 45 °C to the loss of electrochemically active material, which is caused by the formation of a reconstructed, electrochemically inactive surface. This compares to only ≈40% material loss after 1000 cycles at 22 °C.

The formation of the reconstructed, oxygen-depleted surface results in a growth of the charge-transfer resistance of the NCM-811 CAM, which is also reflected by an analogous increase of the DCIR resistance and further leads to overpotential-induced capacity losses. After 700 cycles at 45 °C, the layer thickness around the primary particles exposed to the electrolyte is estimated to be ≈12–14 nm, reasonably consistent with the literature, while only ≈6 nm are estimated after 1000 cycles at 25 °C. We attribute this difference to the faster kinetics for oxygen removal and/or transition-metal rearrangement at the higher temperature.

The overpotential-induced capacity losses occur in a similar ratio both in the discharged state (i.e., during lithiation of the CAM) and the charged state (i.e., during delithiation of the CAM). Whether these losses are predominantly caused by the increased charge-transfer resistance or by a decreased lithium diffusivity in the bulk phase cannot be finally answered. However, the extent of Li-Ni mixing stays constant at 22 °C and increases only by ≈1%–2% after 700 cycles after 45 °C. Furthermore, we could not observe the emergence of a so-called fatigued phase with a layered structure.

Acknowledgments

Financial support by BASF SE through its Scientific Network on Electrochemistry and Batteries is gratefully acknowledged.

Appendix

Equations used for the capacity loss analysis.—The XPD-derived variation of the lithium content (x_{Li}) over the course of cycling (see Fig. 4) enables the deconvolution of the electrochemically measured capacity loss, $\Delta C_{EC}^{BOT\rightarrow i}$ (in mAh g^{-1}):

$$\Delta C_{EC}^{BOT\rightarrow i} = C_{EC}^{BOT} - C_{EC}^{i} \quad [A\cdot1]$$

which is defined by the difference of the discharge capacity in the ith cycle (C_{EC}^{i}) relative to that at the begin-of-test (C_{EC}^{BOT}). Please note that the following equations were established in our former publication by Friedrich et al., where they are explained in great detail.[9]

The first contribution is the absolute loss of electrochemically active material in the form of a reconstructed, O-depleted surface layer, which can be quantified as $\Delta C_{Material}^{BOT\rightarrow i}$ (in mAh g^{-1}, just like the other loss terms) by the following equation:

$$\Delta C_{Material}^{BOT\rightarrow i} = (C_{XPD}^{i} - C_{EC}^{i}) \cdot \Delta\frac{\Delta x_{Li}^{BOT}}{\Delta x_{Li}^{i}} \quad [A\cdot2]$$

Here, the material loss corresponds to the difference between the theoretically expected capacity inferred from XPD (C_{XPD}^{i}, see Eq. 6) and the actually measured discharge capacity in the ith cycle (C_{EC}^{i}). To reference this difference to BOT, it has to be corrected by the accessible Δx_{Li} ranges between the discharged and charged state (e.g., $\Delta x_{Li}^{i} = x_{Li,dis}^{i} - x_{Li,cha}^{i}$), which typically shrink upon cycling due to the increasing overpotential (i.e., $\Delta x_{Li}^{BOT} > \Delta x_{Li}^{i}$).

The overpotential-induced loss ($\Delta C_{Overpotential}^{BOT\rightarrow i}$) is the second contribution, which can be further divided into capacity losses in the discharged ($\Delta C_{Discharge}^{BOT\rightarrow i}$) and in the charged state ($\Delta C_{Charge}^{BOT\rightarrow i}$):

$$\Delta C_{Overpotential}^{BOT\rightarrow i} = \Delta C_{Discharge}^{BOT\rightarrow i} + \Delta C_{Charge}^{BOT\rightarrow i} \quad [A\cdot3]$$

where by the two individual contributions are calculated according to:

$$\Delta C_{Discharge}^{BOT\rightarrow i} = (x_{Li,dis}^{BOT} - x_{Li,dis}^{i}) \cdot \frac{274\ \text{mAh g}^{-1}}{1.01} \cdot (1 - \Delta C_{Material,rel}^{i}) \quad [A\cdot4]$$

$$\Delta C_{Charge}^{BOT\rightarrow i} = (x_{Li,cha}^{i} - x_{Li,cha}^{BOT}) \cdot \frac{274\ \text{mAh g}^{-1}}{1.01} \cdot (1 - \Delta C_{Material,rel}^{i}) \quad [A\cdot5]$$

by taking the difference of the respective x_{Li} values between BOT and the ith cycle in either the discharged ($x_{Li,dis}^{BOT} - x_{Li,dis}^{i}$) or charged state ($x_{Li,cha}^{i} - x_{Li,cha}^{BOT}$). Note that for this analysis it is irrelevant whether the difference in x_{Li} is due to an increase of the CAM's R_{CT} (caused by the formation of a resistive surface layer) or a decrease of the lithium diffusivity in the bulk of the CAM (caused by transition-metal migration into the lithium layer). Since only the electrochemically active material can undergo a capacity loss due to an increasing overpotential, Eqs. A·3–A·5 include a correction term that considers the NCM-811 phase fraction which has already been lost until the ith cycle ($\Delta C_{Material,rel}^{i}$, see Eq. 5).

ORCID

Benjamin Strehle https://orcid.org/0000-0001-8878-1160
Franziska Friedrich https://orcid.org/0000-0001-9400-1212
Hubert A. Gasteiger https://orcid.org/0000-0001-8199-8703

References

1. G. Zubi, R. Dufo-López, M. Carvalho, and G. Pasaoglu, *Renew. Sustain. Energy Rev.*, **89**, 292 (2018).
2. E. A. Olivetti, G. Ceder, G. G. Gaustad, and X. Fu, *Joule*, **1**, 229 (2017).
3. C. Banza Lubaba Nkulu et al., *Nat. Sustain.*, **1**, 495 (2018).
4. H.-J. Noh, S. Youn, C. S. Yoon, and Y.-K. Sun, *J. Power Sources*, **233**, 121 (2013).

5. S.-M. Bak, E. Hu, Y. Zhou, X. Yu, S. D. Senanayake, S.-J. Cho, K.-B. Kim, K. Y. Chung, X.-Q. Yang, and K.-W. Nam, *ACS Appl. Mater. Interfaces*, **6**, 22594 (2014).
6. S.-T. Myung, F. Maglia, K.-J. Park, C. S. Yoon, P. Lamp, S.-J. Kim, and Y.-K. Sun, *ACS Energy Lett.*, **2**, 196 (2017).
7. H.-H. Ryu, K.-J. Park, C. S. Yoon, and Y.-K. Sun, *Chem. Mater.*, **30**, 1155 (2018).
8. W. Li, E. M. Erickson, and A. Manthiram, *Nat. Energy*, **5**, 26 (2020).
9. F. Friedrich, B. Strehle, A. T. S. Freiberg, K. Kleiner, S. J. Day, C. Erk, M. Piana, and H. A. Gasteiger, *J. Electrochem. Soc.*, **166**, A3760 (2019).
10. M.-T. F. Rodrigues, G. Babu, H. Gullapalli, K. Kalaga, F. N. Sayed, K. Kato, J. Joyner, and P. M. Ajayan, *Nat. Energy*, **2**, 17108 (2017).
11. G. Xu, X. Liu, A. Daali, R. Amine, Z. Chen, and K. Amine, *Adv. Funct. Mater.*, **30**, 2004748 (2020).
12. USABC, USABC Goals for Advanced Batteries for EVs (2020), https//www.energy.gov/sites/prod/files/2014/05/f15/APR13_Energy_Storage_d_III_Adv_Battery_Dev_0.pdf.
13. J. Li, J. Harlow, N. Stakheiko, N. Zhang, J. Paulsen, and J. Dahn, *J. Electrochem. Soc.*, **165**, A2682 (2018).
14. R. Jung, P. Strobl, F. Maglia, C. Stinner, and H. A. Gasteiger, *J. Electrochem. Soc.*, **165**, A2869 (2018).
15. S. Schweidler, L. de Biasi, G. Garcia, A. Mazilkin, P. Hartmann, T. Brezesinski, and J. Janek, *ACS Appl. Energy Mater.*, **2**, 7375 (2019).
16. J. E. Harlow et al., *J. Electrochem. Soc.*, **166**, A3031 (2019).
17. C. P. Aiken, J. E. Harlow, R. Tingley, T. Hynes, E. R. Logan, S. L. Glazier, A. S. Keefe, and J. R. Dahn, *J. Electrochem. Soc.*, **167**, 130541 (2020).
18. D. Pritzl, S. Solchenbach, M. Wetjen, and H. A. Gasteiger, *J. Electrochem. Soc.*, **164**, A2625 (2017).
19. *MIMS Client, Version 1.4* (Maccor Inc, Tulsa, United States of America) (2019).
20. *TOPAS-Academic* V6 (Coelho Software, Brisbane, Australia) (2016).
21. P. W. Stephens, *J. Appl. Crystallogr.*, **32**, 281 (1999).
22. O. Dolotko, A. Senyshyn, M. J. Muhlbauer, K. Nikolowski, F. Scheiba, and H. Ehrenberg, *J. Electrochem. Soc.*, **159**, A2082 (2012).
23. R. Morasch, B. Suthar, and H. A. Gasteiger, *J. Electrochem. Soc.*, **167**, 100540 (2020).
24. J. Landesfeind, D. Pritzl, and H. A. Gasteiger, *J. Electrochem. Soc.*, **164**, A1773 (2017).
25. S. Oswald, D. J. Pritzl, M. Wetjen, and H. Gasteiger, *J. Electrochem. Soc.* (2020).
26. S. Meini, M. Piana, H. Beyer, J. Schwämmlein, and H. A. Gasteiger, *J. Electrochem. Soc.*, **159**, A2135 (2012).
27. I. Buchberger, S. Seidlmayer, A. Pokharel, M. Piana, J. Hattendorff, P. Kudejova, R. Gilles, and H. A. Gasteiger, *J. Electrochem. Soc.*, **162**, A2737 (2015).
28. L. M. Thompson, W. Stone, A. Eldesoky, N. K. Smith, C. R. M. McFarlane, J. S. Kim, M. B. Johnson, R. Petibon, and J. R. Dahn, *J. Electrochem. Soc.*, **165**, A2732 (2018).
29. F. T. Wagner, B. Lakshmanan, and M. F. Mathias, *J. Phys. Chem. Lett.*, **1**, 2204 (2010).
30. R. Sharabi, E. Markevich, V. Borgel, G. Salitra, D. Aurbach, G. Semrau, M. A. Schmidt, N. Schall, and C. Stinner, *Electrochem. Commun.*, **13**, 800 (2011).
31. T. Yim, H.-J. Ha, M.-S. Park, K. J. Kim, J.-S. Yu, and Y.-J. Kim, *RSC Adv.*, **3**, 25657 (2013).
32. R. Jung, M. Metzger, F. Maglia, C. Stinner, and H. A. Gasteiger, *J. Electrochem. Soc.*, **164**, A1361 (2017).
33. J. Wandt, A. T. S. Freiberg, A. Ogrodnik, and H. A. Gasteiger, *Mater. Today*, **21**, 825 (2018).
34. S. Solchenbach, G. Hong, A. T. S. Freiberg, R. Jung, and H. A. Gasteiger, *J. Electrochem. Soc.*, **165**, A3304 (2018).
35. R. Jung, F. Linsenmann, R. Thomas, J. Wandt, S. Solchenbach, F. Maglia, C. Stinner, M. Tromp, and H. A. Gasteiger, *J. Electrochem. Soc.*, **166**, A378 (2019).
36. R. Pan, D. Rau, Y. Moryson, J. Sann, and J. Janek, *ACS Appl. Energy Mater.*, **3**, 6065 (2020).
37. T. Teufl, D. Pritzl, S. Solchenbach, H. A. Gasteiger, and M. A. Mendez, *J. Electrochem. Soc.*, **166**, A1275 (2019).
38. R. Jung, M. Metzger, F. Maglia, C. Stinner, and H. A. Gasteiger, *J. Phys. Chem. Lett.*, **8**, 4820 (2017).
39. M. Metzger, P. Walke, S. Solchenbach, G. Salitra, D. Aurbach, and H. A. Gasteiger, *J. Electrochem. Soc.*, **167**, 160522 (2020).
40. A. T. S. Freiberg, M. K. Roos, J. Wandt, R. de Vivie-Riedle, and H. A. Gasteiger, *J. Phys. Chem. A*, **122**, 8828 (2018).
41. T. Teufl, D. Pritzl, P. Krieg, B. Strehle, M. A. Mendez, and H. A. Gasteiger, *J. Electrochem. Soc.*, **167**, 110505 (2020).
42. R. Weber, A. J. Louli, K. P. Plucknett, and J. R. Dahn, *J. Electrochem. Soc.*, **166**, A1779 (2019).
43. H. Li, M. Cormier, N. Zhang, J. Inglis, J. Li, and J. R. Dahn, *J. Electrochem. Soc.*, **166**, A429 (2019).
44. W. Li, X. Liu, Q. Xie, Y. You, M. Chi, and A. Manthiram, *Chem. Mater.*, **32**, 7796 (2020).
45. C. Xu et al., *Nat. Mater.*, **20**, 84 (2020).
46. L. Yin et al., *Chem. Mater.*, **32**, 1002 (2020).
47. Y. Makimura, T. Sasaki, T. Nonaka, Y. F. Nishimura, T. Uyama, C. Okuda, Y. Itou, and Y. Takeuchi, *J. Mater. Chem. A*, **4**, 8350 (2016).
48. K. Kleiner, D. Dixon, P. Jakes, J. Melke, M. Yavuz, C. Roth, K. Nikolowski, V. Liebau, and H. Ehrenberg, *J. Power Sources*, **273**, 70 (2015).
49. H. Liu, M. Wolf, K. Karki, Y.-S. Yu, E. A. Stach, J. Cabana, K. W. Chapman, and P. J. Chupas, *Nano Lett.*, **17**, 3452 (2017).
50. P. Yan, J. Zheng, M. Gu, J. Xiao, J.-G. Zhang, and C.-M. Wang, *Nat. Commun.*, **8**, 14101 (2017).
51. H. M. Dahn, A. J. Smith, J. C. Burns, D. A. Stevens, and J. R. Dahn, *J. Electrochem. Soc.*, **159**, A1405 (2012).
52. M. Dubarry, C. Truchot, and B. Y. Liaw, *J. Power Sources*, **219**, 204 (2012).
53. F. Wang, Z. Lin, L. Liu, X. Wei, S. Lin, L. Dai, Y. Wei, C. Liang, and B. Liaw, *J. Electrochem. Soc.*, **167**, 090549 (2020).
54. J. Li, H. Liu, J. Xia, A. R. Cameron, M. Nie, G. A. Botton, and J. R. Dahn, *J. Electrochem. Soc.*, **164**, A655 (2017).
55. S.-M. Bak, K.-W. Nam, W. Chang, X. Yu, E. Hu, S. Hwang, E. A. Stach, K.-B. Kim, K. Y. Chung, and X.-Q. Yang, *Chem. Mater.*, **25**, 337 (2013).
56. T. Teufl, B. Strehle, P. Müller, H. A. Gasteiger, and M. A. Mendez, *J. Electrochem. Soc.*, **165**, A2718 (2018).
57. L. de Biasi, A. O. Kondrakov, H. Geßwein, T. Brezesinski, P. Hartmann, and J. Janek, *J. Phys. Chem. C*, **121**, 26163 (2017).
58. L. Zou, W. Zhao, H. Jia, J. Zheng, L. Li, D. P. Abraham, G. Chen, J. R. Croy, J.-G. Zhang, and C. Wang, *Chem. Mater.*, **32**, 2884 (2020).
59. S. Ahmed et al., *ACS Nano*, **13**, 10694 (2019).
60. J. Li, H. Li, W. Stone, R. Weber, S. Hy, and J. R. Dahn, *J. Electrochem. Soc.*, **164**, A3529 (2017).
61. J. Li, A. R. Cameron, H. Li, S. Glazier, D. Xiong, M. Chatzidakis, J. Allen, G. A. Botton, and J. R. Dahn, *J. Electrochem. Soc.*, **164**, A1534 (2017).
62. H. H. Sun, H.-H. Ryu, U.-H. Kim, J. A. Weeks, A. Heller, Y.-K. Sun, and C. B. Mullins, *ACS Energy Lett.*, **5**, 1136 (2020).